chemengineering

MDPI

Review

Metal Oxides Applied to Thermochemical Water-Splitting for Hydrogen Production Using Concentrated Solar Energy

Stéphane Abanades

Processes, Materials, and Solar Energy Laboratory, PROMES-CNRS, 7 Rue du Four Solaire, 66120 Font Romeu, France; stephane.abanades@promes.cnrs.fr; Tel.: +33-0468307730

Received: 17 May 2019; Accepted: 2 July 2019; Published: 4 July 2019

Abstract: Solar thermochemical processes have the potential to efficiently convert high-temperature solar heat into storable and transportable chemical fuels such as hydrogen. In such processes, the thermal energy required for the endothermic reaction is supplied by concentrated solar energy and the hydrogen production routes differ as a function of the feedstock resource. While hydrogen production should still rely on carbonaceous feedstocks in a transition period, thermochemical water-splitting using metal oxide redox reactions is considered to date as one of the most attractive methods in the long-term to produce renewable H_2 for direct use in fuel cells or further conversion to synthetic liquid hydrocarbon fuels. The two-step redox cycles generally consist of the endothermic solar thermal reduction of a metal oxide releasing oxygen with concentrated solar energy used as the high-temperature heat source for providing reaction enthalpy; and the exothermic oxidation of the reduced oxide with H_2O to generate H_2. This approach requires the development of redox-active and thermally-stable oxide materials able to split water with both high fuel productivities and chemical conversion rates. The main relevant two-step metal oxide systems are commonly based on volatile (ZnO/Zn, SnO_2/SnO) and non-volatile redox pairs (Fe_3O_4/FeO, ferrites, CeO_2/$CeO_{2-\delta}$, perovskites). These promising hydrogen production cycles are described by providing an overview of the best performing redox systems, with special focus on their capabilities to produce solar hydrogen with high yields, rapid reaction rates, and thermochemical performance stability, and on the solar reactor technologies developed to operate the solid–gas reaction systems.

Keywords: hydrogen; solar energy; water-splitting; thermochemical; two-step cycles; redox materials; metal oxides; solar fuel; solar reactor

1. Introduction

Solar thermochemical processes are efficient routes for converting high temperature solar heat into valuable and sustainable chemical energy carriers (solar fuels). Thermochemical water-splitting cycles consist of the thermal conversion of water into separate streams of hydrogen and oxygen via a series of endothermic and exothermic chemical reactions. It is particularly attractive due to the abundance, availability and low cost of the water feedstock. Endothermic reactions can be driven by high-temperature concentrated solar thermal energy [1–4]. A thermochemical water-splitting cycle operates at much lower working temperatures than direct water thermolysis while resulting in the same global water decomposition reaction.

The interest in thermochemical water-splitting cycles boomed in the late 70s and early 80s with the oil crisis [5–9], and most of the cycles were proposed for being combined with a primary nuclear energy source, thereby imposing constraints on the operating temperature that should remain below 900 °C. Although several hundred cycles have been proposed, only a few has been subjected to substantial

research, and the demonstration of technical feasibility and potential for high efficiency has been barely carried out. In previous studies dealing with screening and evaluation of thermochemical cycles, the maximum cycle temperature level corresponded to the deemed optimum for an advanced high-temperature Generation IV nuclear reactor (e.g. high-temperature gas-cooled reactor HTGR, very-high-temperature reactor VHTR), i.e. about 850 °C [10]. Processes involving higher temperatures were eliminated. A large research effort has mainly been focused on UT-3 and Iodine-Sulphur (I-S) cycles [10–16], in which the primary energy input was the high-temperature heat released from an advanced nuclear reactor (4th generation power station). These cycles have also been proposed in combination with a solar energy source [17–22]. The medium temperature I-S and hybrid sulphur (Westinghouse) cycles that may use either solar or nuclear heat have been examined (e.g., EU-projects HYTHEC (FP6), HycycleS (FP7) and SOL2HY2 (FCH JU)). In particular, the solar decomposition of H_2SO_4 above 850 °C involved in both cycles was studied [17]. Regarding the hybrid sulphur cycle (Ispra Mark 11), sulphuric acid is decomposed in the first reaction at a high temperature to generate sulphur dioxide and oxygen (that can be separated and valorized as byproduct). Sulphur dioxide is then electrolyzed with water at about 80 °C in the second reaction forming hydrogen and fresh sulphuric acid to be recycled back to the first reaction. This electrolysis step requires only about one tenth of the electrical power needed for conventional water electrolysis, thereby reducing the global process energy demand for hydrogen production, which is crucial for future industrial technology commercialization. However, such complex cycles operating below 1000 °C usually involve incomplete reactions or electrochemical steps (hybrid cycles), additional separation steps, hazardous or corrosive reactants and/or products, which results in materials issues for reactor construction and may compromise viable commercial process implementation.

Significant progress has recently been achieved regarding solar energy collectors and concentrators while enabling to reach solar powers of several dozens of megawatts. In this context, more efficient cycles with a lower number of steps should now be suited for operation in a broader range of temperature from 1000 °C to 2000 °C. Short two-step solar-driven cycles are particularly attractive owed to their operational simplicity favoring easier process scale implementation, thus offering the potential for safe, low-cost, and large-scale production of H_2 as a clean energy carrier [23,24]. The cycles based on non-toxic metal oxides [25–29] using process heat at temperature above 1000 °C are the simplest and most promising routes for solar H_2 production.

The solar thermochemistry governing two-step water-splitting cycles involves metal oxide redox reactions. In the first step driven by concentrated solar energy, the reduction of the metal oxide leads to both oxygen release and material activation. In the second water-splitting step, oxidation of the redox-active material (reduced valence state of the metal oxide) with water steam produces hydrogen (Figure 1). A few redox cycles have been investigated for solar hydrogen production from water-splitting. The generic two-step process that makes use of metal oxides redox pairs is based on the following reactions:

$$\text{High temperature reduction step (endothermic):} \quad M_xO_y \rightarrow M_xO_{y-1} + \frac{1}{2}\,O_2 \tag{1}$$

$$\text{Hydrolysis step (exothermic):} \quad M_xO_{y-1} + H_2O \rightarrow M_xO_y + H_2 \tag{2}$$

Such a cycling process presents noticeable advantages: (i) the upper cycle temperature (generally in the range of 1200–1600 °C) is compatible with renewable concentrated solar energy; (ii) water and heat are the only process inputs, hydrogen and oxygen the only chemical outputs; (iii) the produced H_2 and O_2 streams are inherently separated by the different reactions; (iv) the other chemicals and reactants are continually recycled in the closed cycle; (v) the produced H_2 is pure for being directly processed, for instance using a polymer electrolyte membrane fuel cell (PEMFC).

Conventional electrolysis, representing the state-of-the-art technology, also generates pure H_2, but this approach is limited by thermodynamic inefficiencies and has low overall energy conversion efficiency as it requires first the generation of electricity (global energy conversion efficiency below

20% when taking into account the electricity production efficiency). Thermochemical water-splitting cycles are expected to reach higher efficiency than water electrolysis since their energy efficiency is not impaired by the intermediate conversion of heat to electricity. Benchmark is the alkaline water electrolysis using solar electricity generated by either photovoltaics (PV) or concentrating solar power (CSP). With currently available technologies, the overall solar-to-hydrogen energy conversion efficiency reaches 10–14%, when assuming 70% efficiency for electrolysis and 15% (PV) to 20% (CSP) annual efficiency for solar-produced electricity [30]. On the other hand, direct thermal splitting of water would require temperatures exceeding 2000–2500 °C to yield significant amounts of hydrogen. Therefore, thermochemical cycles are proposed to lower the maximum process temperature to a technical manageable level.

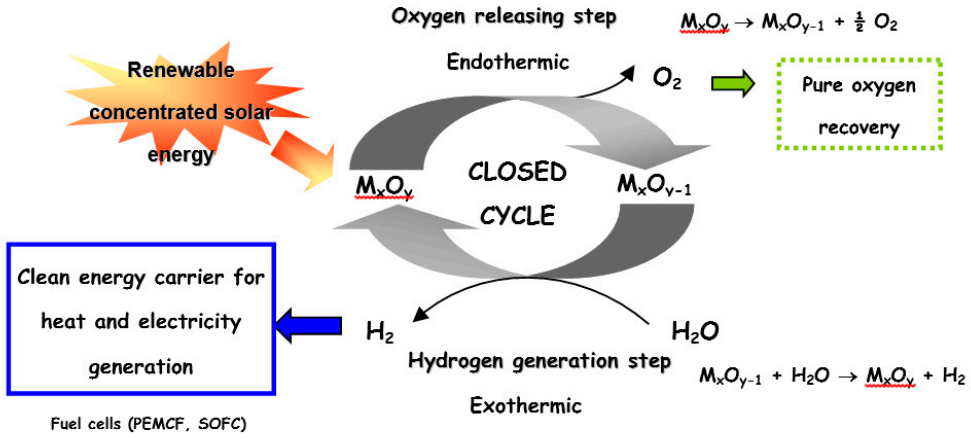

Figure 1. Scheme of the two-step water-splitting cycle based on the M_xO_y/M_xO_{y-1} system.

The cycles working in the temperature range of 900–2000 °C were not considered in previous screening studies [10], because they were not practically compatible with the operating temperature of advanced nuclear reactors. In contrast, they can be plainly considered for a coupling with concentrating solar thermal as primary energy source. Therefore, a new screening, selection, and evaluation of the most promising solar-driven thermochemical cycles for H_2 production was conducted [28]. A database including over 280 referenced thermochemical cycles was constructed at CNRS-PROMES laboratory (France) from a detailed bibliographic survey to sort out the cycles previously proposed in the literature. The developed database incorporates the detailed information on the processing conditions, involved chemical reaction steps, bibliographic references data describing or referring to the cycles. The numerous listed cycles can be classified into a restricted number of defined subcategories (sulphur, iodine, chlorine, bromine, carbon, miscellaneous, hybrid). Objective screening criteria were defined and applied to decrease the number of investigated cycles to a manageable number and to identify potentially applicable solar-driven cycles.

Roughly 30 interesting cycles were selected for further investigations by using a set of defined criteria: (1) upper temperature of the cycle for being compatible with solar concentrating systems, (2) number of reactions and separation steps, (3) number of chemical elements, (4) nature of the cycle (either purely thermal or hybrid thermo-electrochemical), (5) thermodynamics, (6) technical operational feasibility of the cycle accounting for reaction kinetics and chemical conversion yields, (7) expected cycle exergy efficiency, (8) availability and cost of process chemicals and reactants, (9) corrosiveness, (10) presence of non-stationary solid reactants, (11) environmental safety and health issues, (12) type/availability/cost and ease for implementing the separation steps. Chiefly, two and three-step cycles were retained due to their ease of process implementation and integration that should imply favorable process economics. In addition, these cycles basically involve low number of reactions and separation steps (thereby lowering penalties associated with heat transfer limitations and

products separation), available, low-cost, and safe (non-toxic) materials, and a heat input temperature (900–2000 °C) compatible with concentrated solar energy.

The cycles that were eliminated did not respond to the above criteria, as it was the case for those requiring very high temperatures (higher than 2200 °C) (MoO_2/Mo, SiO_2/SiO, WO_3/W), hybrid cycles involving an electrochemical step (Cu-Cl cycle [31,32]), cycles based on toxic (Cd, Hg, or bromide) or corrosive compounds such as potassium hydroxide, cycles that necessitate advanced gas separation techniques (such as membrane technologies), or cycles for which thermodynamics is not favorable such as most cycles based on sulphates [33,34] or chlorine [35–38]. In addition, a method of exergy analysis was developed to determine the exergy requirements and the global exergy efficiency of each selected thermochemical cycle [28]. This method was used to compare the cycles and to identify the main operations responsible for irreversibilities, which is a thermodynamic tool for future process optimization. Energy efficiency analyses related to process implementation in large-scale solar tower chemical plants were conducted [29] to estimate the global solar-to-hydrogen energy conversion efficiency that was about 20% for iron and zinc oxide cycles using currently available data (including the different heat losses taking place in the main process sub-systems comprising solar concentrating system for solar energy collection, solar receiver and reactor, and chemical cycling process).

The research investigations regarding high-temperature cycles were mainly focused on CdO/Cd [39], ZnO/Zn [40–76], SnO_2/SnO [76–82], Mn_2O_3/MnO [83], CeO_2/Ce_2O_3 [84–86], and Fe_3O_4/FeO [87–95]. The utilization of mixed metal oxides (e.g. Zn-ferrite, Mn-ferrite, or Ni-ferrite cycles [96–127]) decreases the temperature of the solar activation step (O_2 release) while the reduced oxide still remains active for the H_2 generation step. Due to their promising growing interest, increasing research activities devoted to the investigation of solar-driven two-step cycles (ZnO/Zn, SnO_2/SnO, Mn_2O_3/MnO, Fe_3O_4/FeO, ferrites, CeO_2/$CeO_{2-\delta}$, perovskites) have been conducted mainly in Switzerland (ETHZ, PSI [40]), Germany (DLR [122]), France (CNRS-PROMES [28]), USA (DOE projects [53,54]) and Japan (Tokyo Institute of Technology [97] and Niigata University [114]).

The current studies are mainly related to thermochemical systems based on metal oxide redox pairs as chemical intermediates. The two-step cycles commonly rely on volatile (ZnO/Zn, SnO_2/SnO) or non-volatile redox pairs (Fe_3O_4/FeO, CeO_2/$CeO_{2-\delta}$, and mixed oxides). The products of the high-temperature reduction reaction are in the gaseous state for the volatile oxide cycle category, whereas redox reactions proceed in the condensed state for the non-volatile oxides.

2. Volatile Metal Oxide Cycles

2.1. ZnO/Zn Cycle

The ZnO/Zn cycle is classified as a volatile oxide cycle because the reduced zinc metal species produced during the decomposition reaction ($ZnO(s) \rightarrow Zn(g) + \frac{1}{2}O_2$) is released from the reactor as a gaseous product. This system has been studied extensively and it is considered as one of the most attractive candidate cycles for being coupled with a solar energy source at high temperature. ZnO can be dissociated near 1800 °C in a solar reactor [58] and Zn is recovered at the reactor exit after rapid quenching the gaseous products. The reported activation energies of the ZnO dissociation varied in the range 312–376 kJ/mol [43,44]. The products recombination between Zn and O_2 represents a parasitic reverse reaction that limits the Zn yield from the solar step [49]. Above the Zn condensation temperature, Zn recombination is controlled by diffusion of Zn(g) and O_2 to the reactor walls [62]. The condensation of Zn vapor in the presence of O_2 was studied by fractional crystallization in a temperature-gradient tube furnace, which revealed that Zn oxidation is predominantly a heterogeneous process and, in the absence of nucleation sites, Zn(g) and O_2 can coexist in a metastable state [42]. Otherwise, quenching the products is necessary in order to avoid Zn re-oxidation, which brings process irreversibility (energy losses) and may further introduce complexity issues during large-scale application. The gas quenching aiming to alleviate Zn recombination issue (e.g., via the addition of large amounts of inert gas) constitutes the main challenge of this redox cycle. A fast products

quenching to cool the gas species down to below 900 °C (that corresponds to the Zn(g) condensation temperature) is advocated [41,61]. The quenching efficiency is sensitive to the dilution ratio of Zn(g) in a flow of inert gas [41]. Alternatively, an effective technique for in-situ Zn/O_2 separation directly at high temperatures may also be used to avoid recombination (electrothermal separation methods [128,129]).

The solar thermochemical reactor represents the main key component of solar processes involving water-splitting cycles. A specific research effort must be thus dedicated to suitable reactor design and optimization. The materials used for both the window and the cavity receiver must be carefully chosen as they represent the most sensitive components of solar reactors that are commonly based on either direct or indirect heating of the reactants using concentrated solar energy. Direct heating provides efficient and rapid heat transfer directly to the reacting matter but such reactor technologies must be designed so that to avoid particle deposition on the optical window (case of entrained particles and particle-laden flow). Alternatively, indirect heating via a heat transfer wall requires using high-temperature resistant refractory materials and may suffer from additional heat losses due to indirect heat transfer. Conventional solar reactor designs usually make use of insulated cavity-type blackbody receivers that allow obtaining almost isothermal conditions in the cavity volume and high solar energy absorption efficiencies [57–61]. High-temperature resistant ceramic materials (refractory) are usually employed for lining the inner reactor volume (including both cavity walls and insulation materials).

Different solar reactor configurations designed for ZnO thermal dissociation have been explored in the literature. The first simple type is based on the direct irradiation of a ZnO rod [44]. Such a reactor involves a packed bed or a moving rod of ZnO placed behind a window at the focus of a solar concentrating system. A number of drawbacks arise while operating such a process. First, only the ZnO irradiated surface is solar heated, whereas the underlying ZnO remains at relatively low temperatures, thus inducing radiative heat losses at the surface and temperature gradient through the layer. The reactant surface area exposed to solar flux is weak when compared with a dispersed particulate system, which results in relatively low reaction rates. High re-radiation losses also occur because the reaction does not proceed at fast enough rate to absorb most of the incident solar energy. This in turn reduces the process energy efficiency. Second, the necessary presence of a window requires using a screening stream of inert gas at its surface, in order to both cool it and protect it from products deposition. Any material or dust deposition on the window may result in opaque absorbing regions and subsequent localized overheating and thermal stress, with a possible window melting. Another developed reactor configuration consists of the rotating conical cavity receiver ("ROCA"). A 10 kW prototype and 100 kW pilot were constructed and tested in a high-flux solar furnace [57–61]. The design was based on a windowed cavity receiver that rotates at a high angular velocity. The cavity walls were made of a refractory material (either ZrO_2, HfO_2, or ZnO itself). ZnO was fed in batch pulses by a screw feeder, and the cavity rotation evenly dispersed the ZnO particles throughout the reactor on the cavity walls. Incident solar radiation was absorbed through the window to heat the ZnO particles, and products were swept by inert carrier gas into a cooling zone for rapid quenching. This reactor concept is promising, but may face difficulties and barriers during scale-up. The limitations imposed by the window that was protected by both water-cooling and inert gas purging, could result in a significant decrease of process efficiency due to both conductive and convective heat losses, and energy requirements for inert gas recycling. The cavity rotation further increases mechanical complexity to the high-temperature chemical process, which presents significant engineering challenges and capital costs issues upon scaling-up. Similar to other systems in which a layer of ZnO is directly heated, the lack of particle separation, mixing, and agitation could hinder the kinetics due to heat and mass transfer limitations. In light of the challenges to be faced by these still promising reactor prototype technologies, the use of rapid reaction aerosol flow reactors was considered to obtain rapid ZnO decomposition kinetics while still being scalable with existing chemical engineering technology [53–56]. The small size of particles yields greater surface area for enhancing heat and mass transfer rates, and the increase of this available area enhances the overall rate of surface processes. Such particles dispersed in a gas flow

have been shown to reach extremely high heating rates, on the order of 10^5 K s^{-1}, when exposed to a nearby high temperature hot emitting surface because of their ability to efficiently absorb the radiative heat flux from the surrounding hot walls. The increased heat and mass transfer rates in aerosol systems fasten solid–gas reaction kinetics, lower the global residence time required for converting the particles, and finally make such a solar receiver more efficient. Indirect solar heating of the particles stream by infrared radiation emitted from the surrounding tube walls further eliminates the need for using an optical window. However, low ZnO conversions were obtained (maximum 17%) and particulate products deposition occurred on the walls [54].

The solid metallic Zn powder produced in the solar step may be used in either a fuel cell or battery, or in the exothermal water-splitting reaction to produce pure H_2 and regenerate ZnO that can be recycled back to the solar step. The produced Zn is a solid that can be stored and fed to the hydrolysis reactor during night time or cloudy periods. The H_2 production step of the ZnO/Zn cycle involves a surface hydrolysis reaction between solid Zn particles (or liquid molten Zn) and steam. The Zn hydrolysis was performed and studied with steam bubbling through molten Zn at 500 °C [63], but the reaction rate and Zn conversion were limited by the formation of a ZnO(s) layer around the steam bubbles, thus preventing efficient contact between fresh reactants. The kinetic rates of such a surface reaction are expected to be limited by mass transfer through either the gas boundary layer or the developing ZnO film at the surface. To maximize reaction rates during the off-sun step of the cycle, the use of particles with a high specific surface area is beneficial, thereby reducing the resistance to mass transfer within the particle and through the developing ZnO film.

Most of previous studies focusing on Zn particles hydrolysis reaction have been carried out either using commercial Zn powders [71,72] or Zn produced from solar carbo-thermal ZnO reduction [73]. The Zn conversion achieved in an aerosol flow reactor fed with both water vapor and commercial Zn particles (average particle size of 158 nm) was about 24% at 540 °C with a gas residence time of about 0.6 s [67]. The reaction rate may become negligible because of a low-permeable ZnO layer growing at the particles surface [71]. Non-isothermal thermogravimetric analysis (TGA) with Zn powder dispersed on quartz wool showed that complete Zn conversion could be reached with longer residence times. Regarding Zn obtained from solar carbo-thermal reduction, increasing the temperature of injected steam flow from 200 to 550 °C increased the Zn conversion from 24% to 81% during the fast reaction stage (observed from 400 °C) [73]. Besides, other studies on hydrolysis using an aerosol flow reactor consisted of the intermediate Zn vaporization before steam quenching the Zn vapors to co-produce both H_2 and Zn/ZnO nanoparticles [64–69], but this process suffered from weak particle yield at the outlet and significant particle deposition at the wall. The advantages of hydrolyzing Zn nanoparticles are three-fold: (1) their high specific surface area inherently increases heat and mass transfer, and reaction kinetics (2) their large surface-to-volume ratio favors their complete bulk oxidation, and (3) their possible entrainment by a gas flow is suitable for allowing a simple, continuous, and controllable feeding of Zn reactants and removal of ZnO products. The in-situ formation and steam hydrolysis of entrained Zn nanoparticles in an aerosol (size: 70–100 nm) freshly produced by vapo-condensation allowed reaching 70% H_2 yield [64]. Ernst et al. [66] obtained up to 90% H_2 yield with reactor temperatures in the range 627–1000 °C, however at the expense of weak particle yield downstream.

Finally, steam hydrolysis of Zn-rich solar-produced nanopowder (synthesized in a high temperature solar chemical reactor) results in complete Zn particle conversion at relatively low temperatures (360–500 °C) [74]. Figure 2 shows the time course of Zn conversion during steam hydrolysis. This conversion is obtained from the ratio between the amount of converted Zn and the initial amount of Zn in the powder. The initial presence of ZnO clusters in the particles promotes the Zn oxidation reaction. The complete Zn particle conversion during hydrolysis is due to both the synthesis method and the involved mechanisms during the solar step, which allows the formation of Zn-rich nanoparticles containing ZnO clusters dispersed in the bulk. The ZnO serves as nucleation sites promoting further oxidation during the water-splitting step. Therefore, the solar-produced

Zn nanoparticles containing a fraction of recombined ZnO show better reaction extent than pure Zn particles.

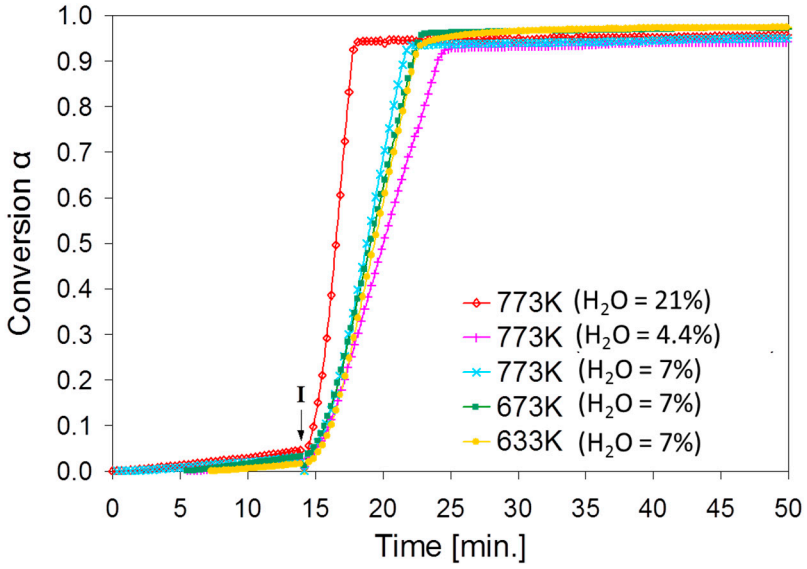

Figure 2. Reaction extents versus time for Zn hydrolysis during isothermal thermogravimetry at different temperatures and steam mole fractions (H_2O mole fraction of 4.4%, 7.0%, or 21%, I corresponds to the time of steam injection at about 14 min) [74].

Assuming an endothermic ZnO decomposition reaction performed at 2000 °C, the energy conversion efficiency of ZnO/Zn cycle reaches about 45% (equal to $HHV_{H2}/\Delta H_{ZnO(25\,°C)\rightarrow Zn(g)+0.5O2(2000\,°C)}$) and the maximum exergy efficiency is 29% without including any heat recovery [40] (defined as the ratio of chemical energy stored in the form of H_2 at ambient temperature to the solar power input, $\eta_{exergy} = -\Delta G^{\circ}_{H2+0.5O2\rightarrow H2O}/Q_{solar}$). Hence, the ZnO/Zn redox system presumably represents one of the most favorable candidate cycles given its potential for achieving both high energy and exergy efficiencies, although significant technical challenges are still remaining and the development of alternative cycles is thus necessary.

2.2. SnO_2/SnO Cycle

More recently, the new SnO_2/SnO redox pair was proposed as an efficient system for two-step water-splitting cycle [77,78] which shares many similar characteristics with the ZnO/Zn system, including: (1) the formation of vapor phase products (volatile oxide) in the solar step, (2) the similar temperature range required for thermal reduction (about 1600–1800 °C at atmospheric pressure), (3) the need for dilution with neutral gas and quenching of the products in the solar step to avoid reverse re-oxidation, and (4) the solar-driven synthesis of reduced SnO particles with nanometric size scale by vapor condensation if a fast enough quenching is applied.

The SnO_2/SnO two-step cycle thus belongs to the class of volatile metal oxide cycles, similarly to ZnO/Zn. The only known cycle based on tin oxides was previously referenced as the "Sn-Souriau" three-step cycle: (i) $SnO_2 \rightarrow SnO + \frac{1}{2}O_2$; (ii) $2SnO \rightarrow Sn + SnO_2$; (iii) $Sn + 2H_2O \rightarrow SnO_2 + H_2$. Nevertheless, the concept of this cycle patented in 1972 [130] was not subjected to any experimental validation to confirm its operational feasibility. Recently, reaction (ii) was proven to reach completion at 600 °C after heating for 10 min under inert gas atmosphere to avoid SnO oxidation. Unfortunately, metallic Sn cannot be separated from SnO_2 by liquefying Sn as advocated in the original "Sn Souriau" cycle, because the molten liquid phase of Sn does not form in the blend. The reaction (iii) generating H_2 from the Sn/SnO_2 mixture issued from disproportionation reaction (ii) is slow and only partial at 600 °C (Sn conversion yield of 45% after 30 min). For the above mentioned reasons, this three-step

cycle was not selected as a promising candidate. Instead, the following innovative SnO_2/SnO two-step cycle was proposed and assessed:

$$\text{Solar reduction step:} \quad SnO_2(s) \rightarrow SnO(g) + \frac{1}{2} O_2 \qquad \text{(endothermic, 1600 °C)} \tag{3}$$

$$\text{Hydrolysis step:} \quad SnO(s) + H_2O(g) \rightarrow SnO_2(s) + H_2 \qquad \text{(exothermic, 550 °C)} \tag{4}$$

The first endothermic solid–gas reaction (ΔH = 557 kJ/mol SnO_2 at 1600 °C) consists of the high temperature thermal reduction of tin(IV) oxide (stannic oxide) into tin(II) oxide (stannous oxide). The required temperature for reaction (3) is suitable for the coupling with a concentrating solar thermal energy source. The SnO product (T_m = 1042 °C, T_b = 1527 °C) is gaseous at the reaction temperature, and SnO(g) is released along with O_2. When the gas temperature drops at the reactor outlet, the gaseous SnO vapors are condensed as nanoparticles via formation of nuclei and particle growth. As for ZnO decomposition, this reaction is also favored by an oxygen partial pressure decrease (via vacuum pumping or inert gas dilution) to limit the reverse recombination reaction with O_2. The beneficial effect of high dilution ratio or reduced pressure operation was demonstrated [49]. A detailed kinetic analysis of the recombination reaction with O_2 was performed. The kinetic parameters were determined for both SnO and Zn recombination (global reaction order of about 1.5 corresponding to the reaction stoichiometry, and activation energies of 42 kJ/mol for SnO and 35 kJ/mol for Zn [49]).

The second solid–gas reaction generating H_2 consists in hydrolyzing SnO nanoparticles by steam water. This moderately exothermic reaction (ΔH = −49 kJ/mol at 500 °C) occurs above 450 °C at atmospheric pressure, with both a satisfactory SnO oxidation rate and a final H_2 yield over 90%. The recovered stannic oxide, SnO_2, is then recycled into the first reaction (solar reduction step), which closes the cycle. The cycle H_2 productivity assuming a complete reactant conversion is 166.3 mL_{H2}/g_{SnO} at normal conditions, which equates to about 14.8 mg_{H2}/g_{SnO} (i.e., the H_2 mass storage capacity of SnO is 1.48 %). The potential applications of such metal oxide systems are related to the stationary or portable generation of H_2. SnO (or Zn) can be long-term stored and transported more easily and surely in the form of solids than H_2, which represents a potential H_2 storage tank. In addition, the reduced species are stable in air and the reactivity of SnO (or Zn) with steam water is not altered even after a long storage period in ambient air. Therefore, on-demand H_2 can be generated at the delivery site when required.

Initially, the SnO hydrolysis was considered as an intermediate step of metallic Sn hydrolysis [131]. Subsequently, the kinetics for hydrolysis of solar-produced SnO particles (and solar Zn for comparison), consisting of nanoparticles synthesized from solar thermal SnO_2 reduction, was studied in details [79–81]. Hydrolysis experiments were carried out to investigate the hydrolysis reaction in a packed-bed reactor and to establish kinetic rate laws. Kinetic parameters encompassing activation energies and reaction orders were determined (122 ± 13 kJ/mol and 2.0 ± 0.3 for SnO, and 87 ± 7 kJ/mol and 3.5 ± 0.5 for Zn, respectively). The reduced SnO species react efficiently in the water-splitting step to generate H_2 in the range of 450–600 °C. The hydrolysis reaction showed a fast initial step at the time of steam injection before the chemical conversion gradually leveled off, which is typical for solid–gas reactions exhibiting a passivating oxide layer growing at the particle surface. The suggested reaction mechanism is composed of a fast reaction-controlled regime during the initial step, followed by a diffusion-controlled regime which increasingly strengthens while the oxide layer is formed at the particle surface. The hydrolysis of solar SnO nanoparticles nearly approached completion (Figure 3), while Zn hydrolysis was fast and reached complete H_2 yield thanks to the nano-sized powders [79]. Further thermogravimetric investigations confirmed SnO conversion approaching 90% at 600 °C [80], but competing reactions such as SnO disproportionation into Sn and SnO_2 occurred concomitantly, as evidenced by Mössbauer spectroscopy [81].

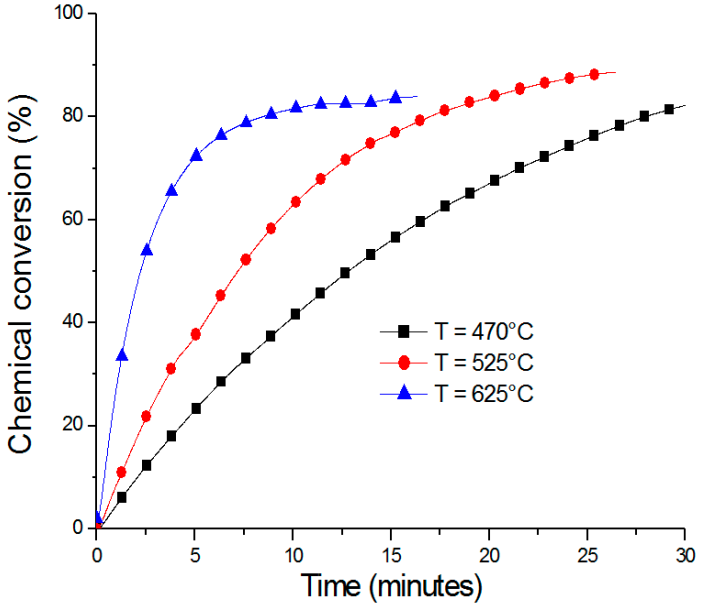

Figure 3. Evolution of chemical conversion during SnO nanoparticles hydrolysis at different temperatures.

The global flow diagram of the thermochemical process integrating the two chemical cycle steps (both solar reactor and hydrolyser) and the H_2 utilization via fuel cell is shown in Figure 4. The produced H_2 is converted in an ideal fuel cell generating both electrical power (W_{FC} = −237 kJ/mol at 25 °C) and heat (Q_{FC} = −49 kJ/mol). The intrinsic energy conversion efficiency of the SnO_2/SnO cycle reaches about 42% accounting for the high heating value of H_2 (HHV_{H2} = 286 kJ/mol). The maximum solar absorption efficiency of a perfectly insulated black-body solar receiver is about 86% at T=1600 °C (assuming a concentration ratio C = 5000 and a direct normal irradiation I = 1 kW/m^2) [132]. Thus, the amount of solar energy input (Q_{solar}) necessary to carry out the endothermic SnO_2 reduction reaction is about 795 kJ/mol, which then allows assessing the global process efficiencies of SnO_2/SnO cycle. The resulting global exergy process efficiency reaches about 29.8% at 1600 °C, which is similar to ZnO/Zn cycle at 2000 °C.

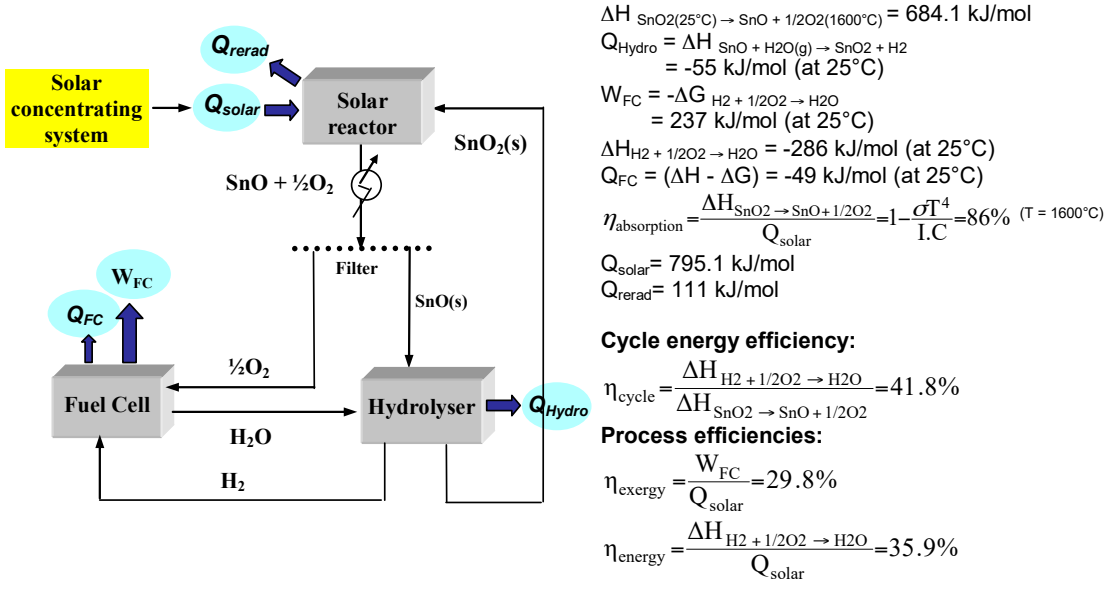

Figure 4. Block diagram of the process and energy efficiency analysis of the two-step SnO_2/SnO thermochemical cycle.

A lab-scale solar reactor prototype (Figure 5) was designed, operated, and simulated for application to the solar thermal reduction of volatile metal oxides involved in the first step of thermochemical cycles. This reactor features a windowed rotating cavity receiver, in which dispersed solid reacting particles are continuously injected by a feeding system [46,47]. The volatile generated products are subsequently recovered at the outlet as nanoparticles agglomerates in a downstream ceramic filter for the subsequent hydrolysis step. The oxide particles injected and dispersed in the directly-irradiated cavity under a controlled inert atmosphere serve simultaneously as both reacting species in the solid–gas decomposition reaction and as radiative absorbers enabling homogeneous heating. The direct particles irradiation provides efficient and rapid heat transfer to the reaction site, thus bypassing the limitations imposed by indirect transfer of high-temperature heat via intermediate absorbing opaque walls. The solar ZnO dissociation was successfully performed as a function of the cavity pressure and inert carrier gas flow-rate, and the obtained Zn product yield in the collected powder reached above 90%. The reaction extent (ZnO conversion) was highly dependent on the particle temperature and the particle conversion increased markedly when the particle temperature slightly increased. Likewise, the conversion increased when decreasing the initial diameter of fed particles according to computational fluid dynamics (CFD) simulations of the reactive gas-particle flow. As a result, complete reaction was predicted when the particles temperature exceeds 1927 °C for initial particle diameter of 1 μm.

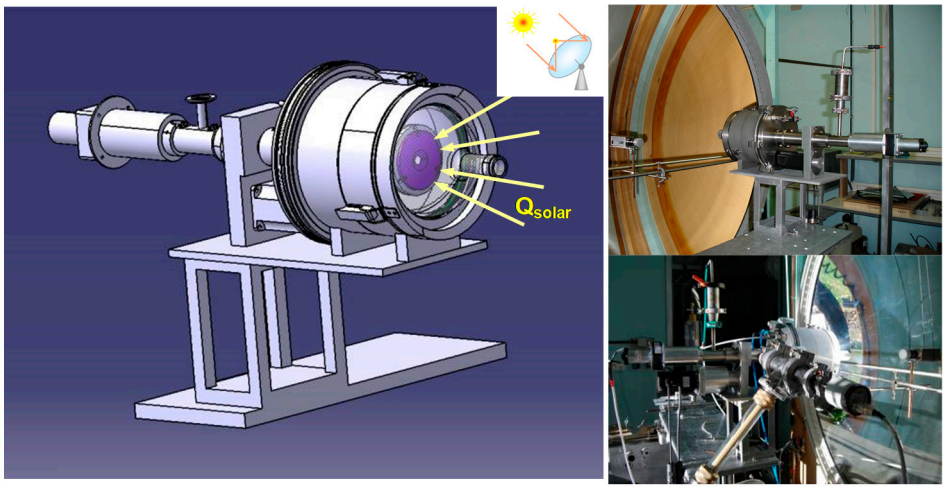

Figure 5. Rotating cavity-type solar reactor designed for continuous volatile metal oxide processing.

Another optimised solar reactor, shown in Figure 6, was then designed enabling the continuous measurement and monitoring of several operating parameters (evolution of temperatures, O_2 concentration at the reactor outlet, Figure 7), and the synthesis of significant amounts of solar Zn and SnO nanopowders (active materials) for the exothermal hydrolysis step [48]. Scanning electron microscopy (SEM) characterizations (Figure 8) show that these powders are composed of agglomerates of nanoparticles (10–50 nm) with a high specific surface area (20–60 m^2/g). This vertical-axis cavity-type solar reactor (1 kW of thermal power absorbed) effects the reaction above 1600 °C at reduced pressure (about 20 kPa) with the compressed oxide reactant injected at the cavity base by the means of an ascending screw piston. This reactor was also used to determine the kinetics of the ZnO and SnO_2 dissociation reactions by fitting reaction models with experimental data [50] thanks to an inverse method involving the online diagnosis of outlet gas combined with a reactor model coupling heat and mass transport phenomena, radiation, and chemical reaction. The activation energy of the oxide dissociation reaction was determined to be 313 ± 31 kJ/mol for ZnO and 353 ± 18 kJ/mol for SnO_2 [50].

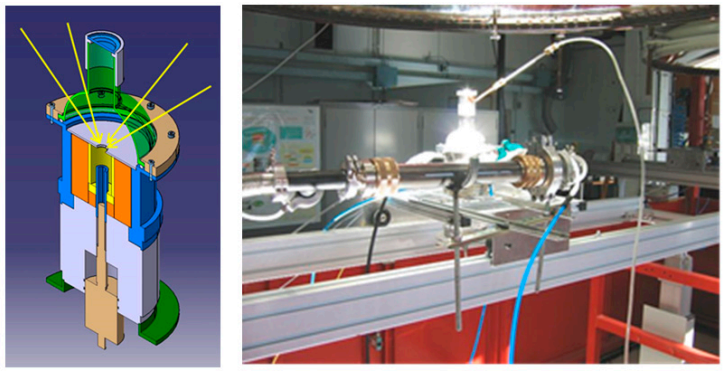

Figure 6. Solar reactor with continuous injection of compressed rod of oxide reactant (ZnO or SnO_2) for nanopowder synthesis (Zn or SnO).

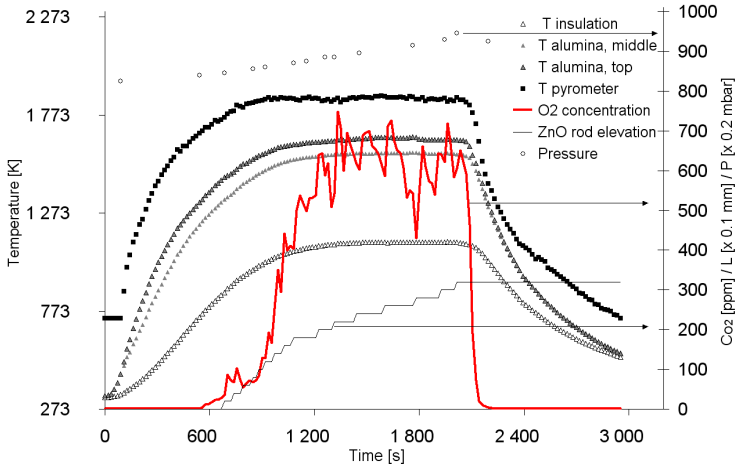

Figure 7. Evolution of temperatures and outlet O_2 concentration measurements in the solar reactor during ZnO dissociation (shutter fully opened at time zero and closed after 2150 s) [48].

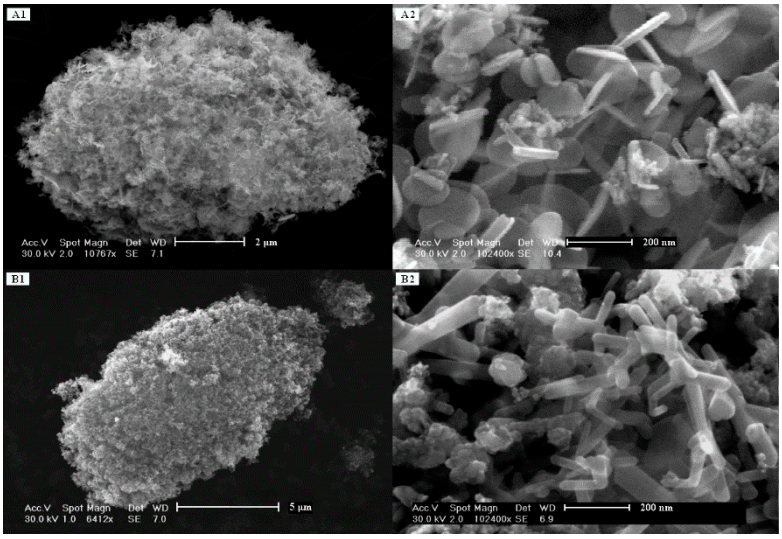

Figure 8. SEM images of solar-produced powders of (**A**) SnO and (**B**) Zn synthesized from solar thermal reduction of corresponding oxides followed by gas quenching.

3. Non-Volatile Metal Oxide Cycles

The iron oxide-based (Fe_3O_4/FeO) two-step cycle is particularly attractive because it features simple reactants and chemical steps (in comparison with nuclear-based cycles) and available safe

reactants (resulting in lower irreversibility inducing potentially superior cycle energy efficiency). Furthermore, it also involves non-corrosive solid materials involved in solid–gas reactions, and it avoids the drawback of potential reverse recombination reaction with O_2 during gas quenching commonly encountered with volatile metal oxides such as zinc, tin or cadmium oxides [62,88]. A key benefit relies on the fact that non-volatile iron oxide systems proceed with the continuous release and removal of the evolved gaseous O_2 from the condensed reacting phase during the solar reduction step, thus promoting high reduction extents. The Fe_3O_4/FeO redox pair was originally proposed by Nakamura [87]. This two-step cycle proceeds as follows:

$$\text{Solar reduction step:} \quad Fe_3O_4(\text{l-s}) \rightarrow 3FeO(\text{l-s}) + 1/2O_2 \tag{5}$$

$$\text{Hydrolysis step:} \quad 3FeO(s) + H_2O(g) \rightarrow Fe_3O_4(s) + H_2 \tag{6}$$

The first high-temperature solar step (thermal reduction of Fe_3O_4) is highly endothermic (ΔH° = 319.5 kJ/mol), whereas the second low-temperature step (FeO hydrolysis) is slightly exothermic (ΔH° = −33.6 kJ/mol). The amount of solar energy theoretically needed to produce 1 mol of H_2 corresponds to the summation of the sensible energy required to heat 1 mol of Fe_3O_4 from 600 °C to 2100 °C (446.51 kJ), the endothermic reduction enthalpy (242.84 kJ), and the energy required to heat and vaporize water from 25°C to 600 °C (64.9 kJ) [126]. On the basis of these temperature levels and the HHV of H_2 (286 kJ/mol), the theoretical energy conversion efficiency of Fe_3O_4/FeO cycle is 37.1%.

The high-temperature solar thermal reduction of magnetite to wüstite theoretically proceeds at temperatures above 2200 °C under 1 bar (according to Gibbs free energy variation) [133]. In addition to stoichiometric FeO, thermodynamics predicts the formation of non-stoichiometric wüstite phases ($Fe_{1-y}O$ such as $Fe_{0.947}O$) (Figure 9). The thermal reduction of magnetite has been experimentally studied [88–94] and demonstrated by using a 2 kW (thermal power) parabolic solar concentrator. The reduction of magnetite was only noticeable at temperatures above the Fe_3O_4 melting point (1597 °C). Tofighi et al. [89,90] showed that a 0.8 g sample reached 80% conversion after 5 min at 2000 °C in an Ar atmosphere (the conversion in air only reaches 40%). Because of the high temperature thermal treatment, the Fe_3O_4 reduction occurs concomitantly with a slight material vaporization. Weidenkaff et al. [92] reported that the exothermic hydrolysis reaction of wüstite with steam water is influenced by the non-stoichiometry, structure and morphology of the parent wüstite phases and by the reaction temperature. The water-splitting hydrolysis reaction using FeO is favorable only below 800 °C (when $\Delta G^\circ < 0$) and the theoretical FeO conversion decreases with increasing temperature according to thermodynamics (Figure 10).

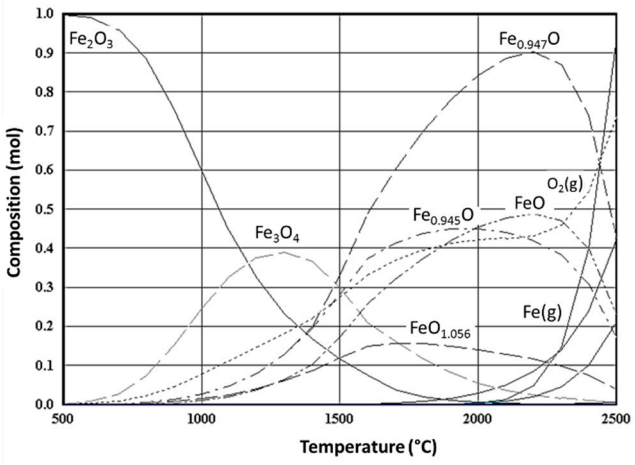

Figure 9. Thermodynamic equilibrium composition of the Fe-O system (1 mol of Fe_2O_3, 100 mol of N_2, P = 1 bar).

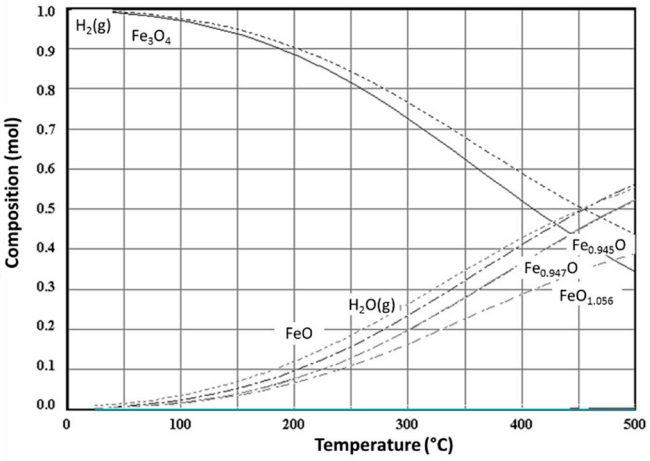

Figure 10. Thermodynamic equilibrium composition of the Fe-O-H system (3 mol of FeO, 1 mol of H_2O, N_2 atmosphere, P = 1 bar).

Besides, the complete thermal reduction of hematite (Fe_2O_3) into wüstite was achieved in a high-temperature solar reactor operated at 1600 °C and 0.1 bar under inert gas atmosphere [93]. The oxygen-releasing reaction proceeds via the formation of the molten oxide and it requires about 2 min to reach completion, which confirms previously reported results. Further TGA experiments confirmed that wüstite formation starts near the Fe_3O_4 melting point (Figure 11). The reduced oxide is thus recovered as a hardened structure that cannot react with water efficiently and the milling of the solar-reduced material into a fine powder is then necessary to carry out the subsequent hydrolysis step.

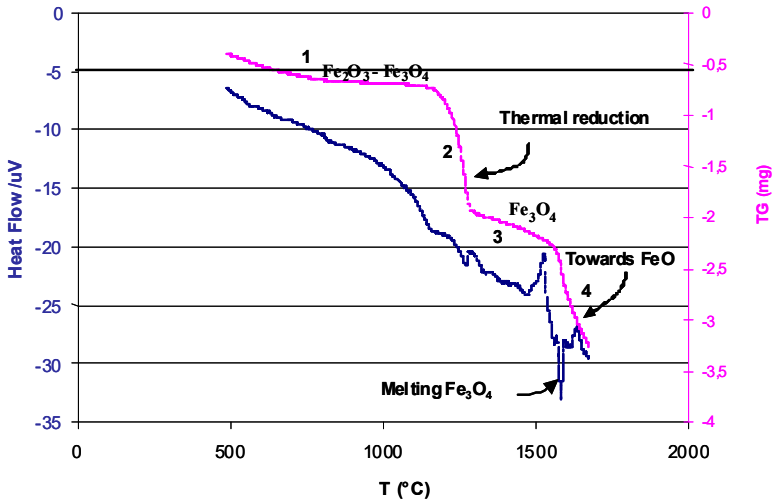

Figure 11. Thermogravimetric analysis TGA (mass loss signal in mg) and differential thermal analysis DTA (heat flow signal in microvolt) of Fe_2O_3 under Ar atmosphere.

A quantitative gas analysis of the amount of H_2 evolved was performed in a continuous way to determine the reaction kinetics and chemical conversion of wüstite hydrolysis. A conversion of 83% was measured regarding the hydrolysis reaction at 575 °C of non-stoichiometric solar-produced wüstite ($Fe_{(1-y)}O$) milled into a fine powder (particle size of 30–50 µm) [93]. The hydrolysis kinetics is dependent on the oxide material physical properties, reaction temperature, and particle size (Figure 12). The reaction rate decreases with time because of the formation of a low permeable oxide layer (Fe_3O_4) at the particles surface, which then grows with time and hinders the reaction. The hydrolysis reaction of particles is governed by two successive controlling phenomena: the fast steam oxidation of the external surface of particle followed by steam diffusion inside the particle pores. The maximum initial hydrolysis reaction rates were achieved for solar-produced wüstite, enabling a bulk hydrogen

production at the beginning of the reaction with steam corresponding to the rapid oxidation of the surface area. The higher reaction rates obtained with solar FeO-rich powders are due to the formation of non-stoichiometric wüstite phases ($Fe_{1-\delta}O$ with δ close to 0.05) during the solar synthesis step. Indeed, solar thermal processing of materials is commonly characterized by high heating and quenching rates favoring formation of defects and cation vacancies in the lattice structure, in turn yielding materials with high contents of non-stoichiometric phases, as validated by thermodynamics predicting the formation of different non-stoichiometric wüstite phases at high temperature. In summary, wüstite hydrolysis is hindered by the formation of a Fe_3O_4 diffusion barrier and the use of fine particles, obtained for instance from an intermediate mechanical particle grinding step, is needed to improve the particle conversion extent. In contrast, the two-step iron oxide cycle (Fe_3O_4/FeO) involves low cost and abundant chemical compounds and could potentially become an attractive option for large-scale H_2 production in future solar processes, thus requiring the design, demonstration and scale-up of efficient and reliable solar reactor technologies.

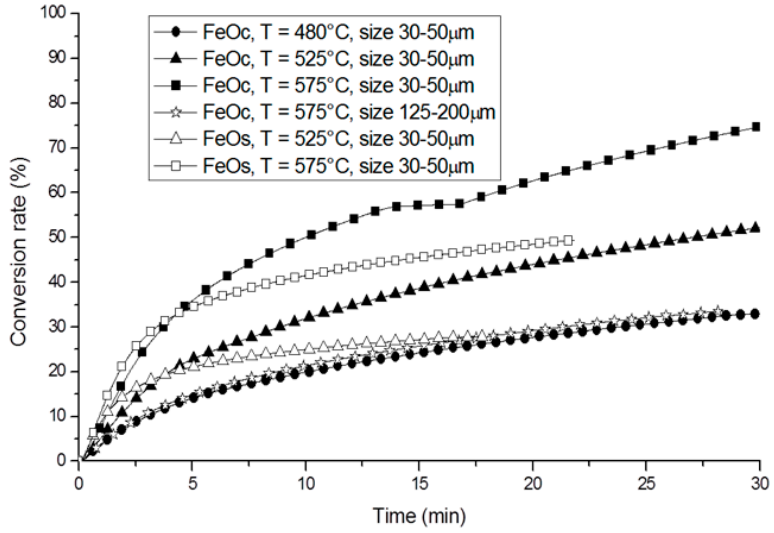

Figure 12. Evolution of chemical conversion rates during continuous FeO hydrolysis producing H_2 as a function of the temperature (FeO_c: commercial FeO, FeO_s: solar-produced FeO) [93].

Regarding other metal-oxide redox systems, most of them are not feasible practically because they require a too much elevated temperature during the solar reduction step ($\Delta G° < 0$ for T > 2200 °C in the case of MoO_2/Mo, SnO_2/Sn, TiO_2/TiO_{2-x}, MgO/Mg, or CaO/Ca redox pairs). In contrast, the non-volatile systems such as Co_3O_4/CoO and Mn_3O_4/MnO redox pairs exhibit a low reduction temperature (902 °C and 1537 °C in air, respectively), but the hydrolysis step is not thermodynamically feasible (thermodynamic calculations predict H_2 yields below 1% for two-step cycles involving these oxides [35,133]).

In order to lower the maximum temperature of the solar reduction step, ferrite cycles were alternatively proposed [97,98]. Oxygen deficient with cation excess Ni-Mn spinel ferrites ($Ni_{0.5}Mn_{0.5}Fe_2O_{4-\delta}$ with δ indicating the oxygen deficiency of the spinel) were proven to be capable for both water-splitting below 800 °C and regeneration (oxygen release) above 800 °C [98]. However, the low water-splitting capability of the (Ni,Mn)-ferrite system was arising from their small content in activated oxygen deficiency (oxygen vacancies) reached in the solid [96]. Strategies for improving the amount of oxygen vacancies in solid compounds have thus been investigated.

The partial substitution of iron by nickel [115], manganese [95], cobalt [114], aluminum-copper [113] or zinc [103–111] in the Fe_3O_4 spinel structure forms mixed iron oxides of general formula $(Fe_{1-x}M_x)_3O_4$. This ferrite can be reduced at much lower temperatures than those required for Fe_3O_4 thermal reduction (thus avoiding melting), while the reduced phase $(Fe_{1-x}M_x)_{1-y}O$ is still capable to perform water-splitting [95]. Allendorf et al. [127] reported detailed thermodynamic analysis applied to ferrites

(MFe_2O_4, with M = Co, Ni, or Zn). Their results point out that the use of ferrites is beneficial because the thermal reduction step is thermodynamically more favorable in comparison with pure iron oxide (Fe_3O_4). Thermodynamics also indicates that Ni-ferrite shows the most favorable combination of both thermal reduction and hydrolysis reaction.

Among many feasible cycles, the Zn/Fe_3O_4 system was able to react with H_2O to form H_2 and $ZnFe_2O_4$ (Zn-ferrite) at 600 °C [103,104]. Nevertheless, to form metallic Zn during the O_2-releasing step, either lowering the O_2 partial pressure or cooling the gas mixture was necessary to avoid metallic Zn oxidation, as for the ZnO/Zn cycle [110]. It was further shown that the H_2 production reaction can be carried out by using both ZnO and Fe_3O_4 to split water, which is thus more attractive since the O_2-releasing step does not require any quenching step and can simply proceed in air at 1500 °C [105].

$$3\ ZnO + 2\ Fe_3O_4 + H_2O \rightarrow 3\ ZnFe_2O_4 + H_2 \qquad T = 600–8000\ °C \tag{7}$$

$$3\ ZnFe_2O_4 \rightarrow 3\ ZnO + 2\ Fe_3O_4 + \frac{1}{2}\ O_2 \qquad T = 1500\ °C \tag{8}$$

As previously observed for the Fe_3O_4/FeO system, mixed iron oxides may similarly undergo rapid deactivation during thermochemical cycling due to coarsening and sintering of the iron oxide particles. The use of refractory ceramics as stable supports can help to alleviate material sintering, and enhance H_2 productivity without deactivation through cyclic reaction. Hence, the ferrite particles were supported on monoclinic ZrO_2 fine particles (m-ZrO_2) that provide a good resistance to agglomeration (densification) and sintering at the working temperatures of 1000–1400 °C, because m-ZrO_2 features a higher melting point than ferrite while being chemically inert to ferrite material at high temperatures. As a result, repeatable and stable thermochemical performance during two-step water-splitting cycles was demonstrated by using active ZrO_2-supported ferrite particles [114–117].

In addition, partially-stabilized tetragonal zirconia (t-PSZ) and yttria-stabilized cubic zirconia (c-YSZ) can also be used as an inert support [112,118]. Thermochemical cycling involving Fe-YSZ particles is suitable to alleviate the iron oxides sintering or melting at high temperatures thanks to the incorporation of active Fe ions into the YSZ crystal lattice, thus resulting in enhanced and reproducible thermochemical performance of the cyclic reaction. The suggested mechanism was based on the fact that the YSZ support can react with particles of ferrite at temperatures above 1400 °C in an inert atmosphere, in turn forming a solid solution. For Fe_3O_4/c-YSZ (ZrO_2 doped with over 8 mol% of Y_2O_3), the following mechanism was proposed [118]:

(1) Formation of Fe^{2+}-YSZ at 1400 °C (under N_2):

$$x/3Fe_3O_4 + Y_yZr_{1-y}O_{2-y/2} \rightarrow {Fe^{2+}}_xY_yZr_{1-y}O_{2-y/2+x} + x/6O_2 \tag{9}$$

(2) Water-splitting at 1000 °C (60 min.) and thermal reduction at 1400 °C (30 min.):

$${Fe^{2+}}_xY_yZr_{1-y}O_{2-y/2+x} + x/2H_2O \rightarrow {Fe^{3+}}_xY_yZr_{1-y}O_{2-y/2+3x/2} + x/2H_2 \tag{10}$$

$${Fe^{3+}}_xY_yZr_{1-y}O_{2-y/2+3x/2} \rightarrow {Fe^{2+}}_xY_yZr_{1-y}O_{2-y/2+x} + x/4O_2 \tag{11}$$

In parallel to the fundamental research on the abovementioned redox working materials, a number of solar chemical reactor concepts have been designed and developed. These include reactors incorporating multi-channel honeycomb structures [122–124] and ceramic foams coated with ferrite [117,118], rotary-type reactors [120,126], and fluidized beds [119].

Further advances on ferrite-based systems have been proposed in the collaborative EU-project HYDROSOL (coordinated by APTL/CERTH from Greece) aiming to operate the complete redox cycle in a single solar receiver/reactor [124]. This reactor features multi-channeled ceramic (siliconized and recrystallized SiC) honeycomb structures coated with active redox materials (iron oxide-based) capable for both water-splitting at 800 °C and regeneration at 1300 °C (temperature-swing cycle). This operational technique using a fixed reactant integrated inside the reactor avoids the need of

continuous particle feeding and collection at the process outlet (no solid flow). The monolithic ceramic structure acts as an efficient volumetric solar absorber. The whole cycling process can be achieved in a single solar energy receiver/converter and it approaches a configuration similar to that encountered in automobile exhaust catalytic converters. The water steam flowing inside the ceramic structure oxidizes the reduced activated material producing pure hydrogen. Then, the material must be reduced during the regeneration step by increasing the solar receiver temperature, allowing a cyclical operation in a single reactor. Various compositions of M-Zn-doped iron oxides (M=Mn or Ni) with a spinel or wüstite phase structure were synthesized via aerosol spray pyrolysis (ASP) and combustion self-propagating high-temperature synthesis (SHS) [124,125], and then used as coatings on the monolith [122]. A pilot-scale (100 kW) solar reactor equipped with two parallel ceramic monolithic supports operating in opposite modes was then developed for quasi-continuous H_2 production [123]. The favored redox systems are zinc- and nickel/zinc-based ferrites. The reaction scheme in the case of zinc can be written as follows:

$$ZnFe^{2+}{}_yFe^{3+}{}_{2-y}O_{4-y/2} + xH_2O \rightarrow ZnFe^{2+}{}_{y-x/2}Fe^{3+}{}_{2-y+x/2}O_{4-y/2+x} + xH_2 \quad (12)$$

$$ZnFe^{2+}{}_{y-x/2}Fe^{3+}{}_{2-y+x/2}O_{4-y/2+x} \rightarrow ZnFe^{2+}{}_yFe^{3+}{}_{2-y}O_{4-y/2} + x/2O_2 \quad (13)$$

Gokon et al. [117,118] proposed and tested ceramic foam materials made of MgO-partially stabilized Zirconia (MPSZ). The porous foam was coated with both c-YSZ and Fe_3O_4 particles (Fe_3O_4/YSZ/MPSZ foam device) and it effectively absorbs solar radiation due to the large specific surface area. The H_2 generation from Fe_3O_4/YSZ/MPSZ foam devices is associated with the redox transition of Fe^{2+}-Fe^{3+} ions in the YSZ lattice. The deactivation of Fe_3O_4 due to high-temperature sintering can be alleviated because the active Fe^{2+} ions remain in the YSZ lattice. The same ceramic foams were used with coatings made of $NiFe_2O_4$/m-ZrO_2 powders that exhibit the highest reactivity among the ferrite/zirconia systems.

Diver et al. [126] developed a concept of counter-rotating ring receiver/reactor/recuperator (CR5) enabling efficient sensible heat recovery during cyclic reactions to reach acceptable thermal efficiencies. The solar-driven heat engine is composed of a stack of counter-rotating rings to which are attached fins made of an active metal oxide ceramic. While the rings rotate, the metal oxide material moves alternately through a high temperature solar reduction zone and a lower temperature water-splitting zone. Since the fins counter-rotate, sensible heat can be internally recovered, thus reducing the overall energy input requirements for the aim of improving efficiencies.

Kaneko et al. [120] also developed a similar concept of rotary-type solar reactor integrating Ni-Mn ferrite loaded on a YSZ support.

Gokon et al. [119] proposed and tested a solar reactor for two-step water-splitting using m-ZrO_2 supported $NiFe_2O_4$ particles processed in an internally circulating fluidized bed. The ferrite particle conversion of approximately 45% was reached upon 1 kW of input simulated power supplied by Xe-beam irradiation. The proposed solar reactor concept was considered to be suited for being associated with beam-down optics [134].

Finally, the two-step cycle based on cerium oxides (CeO_2/Ce_2O_3) was first demonstrated in 2006 by Abanades and Flamant [84], consisting of two chemical steps: (1) solar reduction, $2CeO_2 \rightarrow Ce_2O_3 + 1/2O_2$; (2) hydrolysis, $Ce_2O_3 + H_2O \rightarrow 2CeO_2 + H_2$. CeO_2 was first reduced into Ce_2O_3 during material melting over 2000 °C under inert atmosphere at reduced pressure (10–20 kPa), which induced also a partial sublimation of CeO_2. The reduced material was pounded into powder (50–150 μm) for the hydrolysis tests. Then, an efficient reaction of Ce_2O_3 with water producing H_2 was observed with a rapid and complete oxidation of Ce(III) oxide below 500 °C. The high reactivity of Ce_2O_3 with steam (3 $mmol_{H2}/gCe_2O_3$) was shown to be the main interest of the CeO_2/Ce_2O_3 cycle. This observation opened the door to a new research area related to the mixed oxide cycles containing cerium oxides [135,136]. Similar to ferrite cycles, the targeted result is the significant decrease of the reduction temperature of Ce(IV) into Ce(III) species, while taking advantage of the high reactivity

of Ce(III) species with water (and/or CO_2). Early studies on ceria-based materials synthesis and physicochemical characterization at CNRS-PROMES laboratory (France) showed that binary systems such as CeO_2-ZrO_2 solid solutions can be promising candidates for two-step water-splitting.

The thermodynamic and kinetic properties of ceria can be altered by doping its fluorite structure with transition metals and rare earth metal oxides [135–154]. Indeed, ceria is an active compound used in many catalytic systems, and it is attractive due to its thermal stability (good resistance to sintering) and ability to exchange oxygen via storing and releasing oxygen reversibly. This oxygen mobility is mainly restricted to the material surface unless the ceria is modified by adding another oxide, such as typically zirconia, which favors the material bulk reduction thanks to enhanced oxygen diffusion rates. However, oxidation thermodynamics of Zr-substituted systems are not as favorable as for pure ceria. The addition of dopants in ceria fluorite structure ($M_xCe_{1-x}O_2$, where the added metal M is commonly a trivalent cation like Y^{3+}, La^{3+}, Gd^{3+}, Sm^{3+}, Pr^{3+}, Sc^{3+} or tetravalent cation like Zr^{4+} or Hf^{4+}) shows a favorable impact on the thermodynamics of ceria reduction, and this approach has been extensively investigated for improving the ionic conductivity of solid oxide fuel cells, which is directly linked to the extent of oxygen vacancies. The addition of dopants has been shown to enhance the reduction extent at low oxygen partial pressure when compared with un-doped ceria (at the expense however of lower oxidation capability with water). Hence, the introduction of dopants such as Zr [145–154], Sm [139] and transition metals oxides (MO_x with M = Mn, Ni, Fe, Cu) [135,140,141] has been extensively explored for applications in solar-driven thermochemical redox cycles, as an efficient means to enhance the thermodynamic driving force of the O_2-releasing reduction reaction at lower temperatures. However, it should be noted that trivalent dopants do not improve significantly the thermochemical performance of ceria because they do not present any meaningful increase of the fuel production or improvement of the thermal stability.

The deviation from oxygen stoichiometry (δ in $CeO_{2-\delta}$), otherwise known as the oxygen storage capacity, is directly related to the maximum amount of H_2 capable of being generated during oxidation. While the oxygen exchange capability of ceria is lower compared to iron oxide-based cycles, sintering is less problematic because the melting point is considerably higher. Different research works have evidenced the high promise of ceria for application to solar fuel production according to the redox cycle represented in Figure 13, using various ceria microstructures and morphologies including dispersed powders [140–149], three-dimensionally ordered macroporous (3DOM) powders featuring templated macro-scale porosity [154,155], porous structured monoliths [137–139], porous felts or fibers [156,157], or reticulated porous foams [158–160]. The morphologies enabling both enhanced available geometric surface area and bulk interconnected pore system that facilitate the mass transport of reacting species to and from the oxidation sites, are the most suitable for rapid fuel production. Optimized materials shaping is thus required to provide a good solar absorptivity favoring homogeneous heating, along with a high specific surface area favoring solid–gas reactions. A long-term thermal stability is also required for the considered ceria structures regardless of the involved shaping method. However, the material shaping process represents an additional step required for the preparation of tailored materials and for their incorporation in suitable solar reactors, which could have an impact on the process economics.

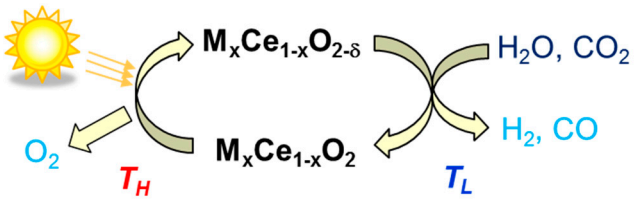

Figure 13. Cycles based on nonstoichiometric oxides (substituted ceria) for syngas production.

The amount of O_2 released during the reduction step (oxygen non-stoichiometry, δ) at 1400 °C and the associated reduction yield depend significantly on the presence and amount of Zr introduced

in the materials [149]. The reduction yields of the materials (Ce^{3+}/Ce_{total}) range from 6% for pure un-doped ceria to 28% for 50%-Zr in Zr-substituted ceria during the first cycle. By increasing the Zr amount in ceria, the reduction yield increases linearly. This result points out the beneficial effect of Zr addition in promoting Ce^{4+} reduction (Figure 14). In contrast, the presence of trivalent dopants has no noticeable effect on the material reducibility and hydrogen production yield.

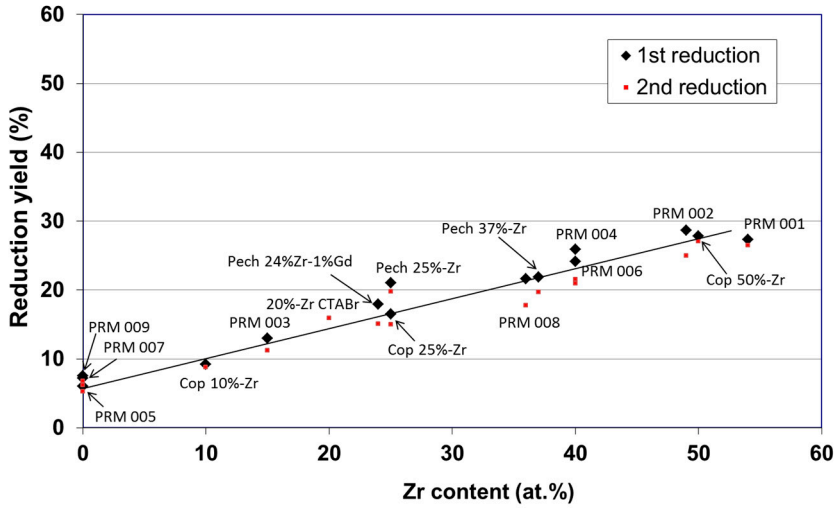

Figure 14. Evolution of the measured reduction yield in ceria-based materials at 1400 °C in Ar as a function of the Zr content [149].

Given that Zr^{4+} cation is not reducible, the gravimetric amount of O_2 released per unit mass of material (thus the potential H_2 production) evolves differently compared to the ceria reduction yield. The materials with Zr content over 25% are the most suitable compounds in term of oxygen availability and mobility. The Figure 15 represents the evolution of the O_2 amount released from the ceria materials during the reduction step as a function of the Zr content. In contrast to the evolution of the reduction yield (Figure 14), the gravimetric amount of O_2 released tends to reach a plateau above roughly 25% of Zr content. The quantity of oxygen released reaches a threshold because a balance settles: the reduction yield is indeed increased whereas the number of reducible cation (Ce^{4+}) in ceria/zirconia solid solution is concomitantly decreased when increasing the Zr content.

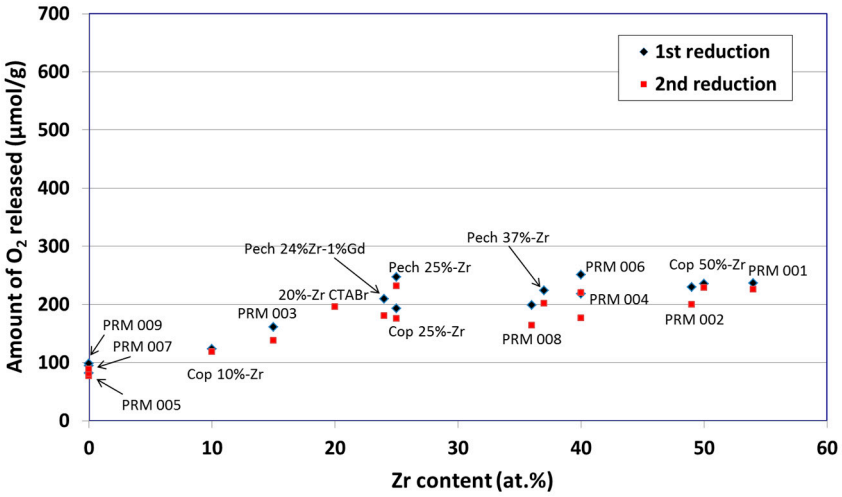

Figure 15. Evolution of the measured amount of oxygen released during the reduction step at 1400 °C in Ar as a function of the Zr content [149].

The steam hydrolysis of the Zr-substituted ceria powders was also studied as a function of the reaction temperature (850 °C, 950 °C, and 1050 °C) for 25%-Zr content and a reduction temperature in the previous step of 1400 °C. The H_2/O_2 ratio increases with temperature and equals two at 1050 °C with a final amount of H_2 produced of 240 µmol/g (Figure 16). The kinetic parameters based on Arrhenius law have been identified from these isothermal experiments and the obtained activation energy was found to be 51 kJ/mol for the hydrolysis reaction [145].

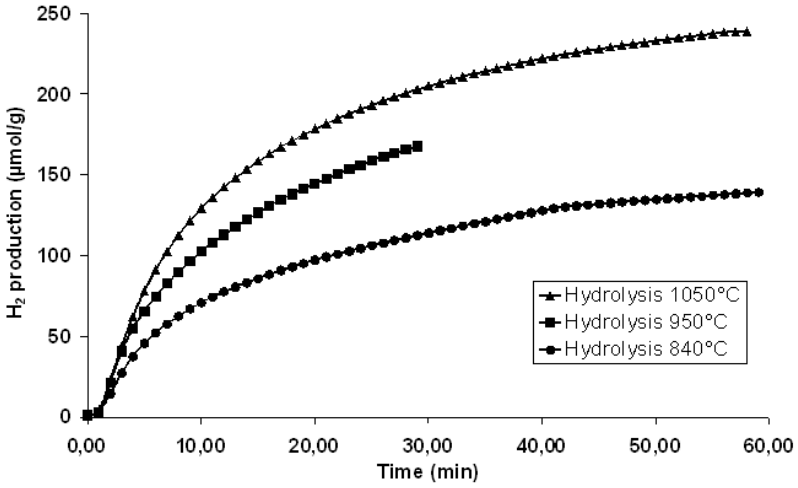

Figure 16. Production of hydrogen at different temperatures during steam hydrolysis of Zr-substituted ceria (25%-Zr) [145].

More recently, perovskites of the form $ABO_{3-\delta}$ have emerged as a new attractive class of nonstoichiometric oxides that are widely unexplored for thermochemical cycles [161–173]. These oxygen-deficient materials exhibit interesting characteristics concerning oxygen storage capacities and transport properties through oxygen vacancies formation. Dopants can be substituted on both A and B cation sites, and thus the number of potential material configurations is substantially greater than for ceria-based systems. Elevated water-splitting activity has been demonstrated in $La_{1-x}Sr_xMnO_{3-\delta}$ materials, so-called LSM (lanthanum strontium manganite) perovskites (Figure 17) [166], and H_2 fuel production performance comparing favorably to that of CeO_2 has been evidenced in Sr- and Mn-substituted $LaAlO_3$ [173], with H_2 productions (up to around 300 µmol/g with $Sr_xLa_{1-x}Mn_yAl_{1-y}O_{3-\delta}$ for one cycle with thermal reduction at 1350 °C and oxidation at 1000 °C) that are only slightly lower than those measured for Zr-substituted ceria. The controlled introduction of Sr into $LaMnO_3$ allows for tuning the redox thermodynamics in the $La_{1-x}Sr_xMnO_3$ compositional series. Decreasing the amount of substituted Sr in LSM enhanced the re-oxidation yield at the expense of a lowered final reduction extent (lower δ), thus decreasing the global amount of generated H_2. The rate of hydrogen production decreased when increasing Sr content, confirming that the intermediate materials formulations offer the most favorable combination of redox properties with trade-off between reduction and oxidation thermodynamics. The observed evolution of the Mn oxidation state during cycles in manganite perovskites implied that partial re-oxidation of Mn^{3+} into Mn^{4+} occurred, thus highlighting the activation of Mn^{4+}/Mn^{3+} redox pair in the perovskites (whereas it is not active in Mn_2O_3/Mn_3O_4). Based on the possible number of doping schemes, series of even more attractive materials certainly remain to be discovered.

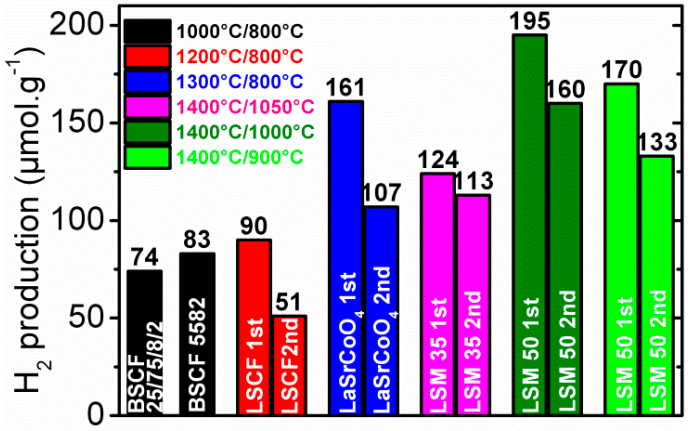

Figure 17. Summary of the hydrogen produced after the first and second water-splitting step and determined from TG analysis for different perovskite compounds as function of temperatures of reduction/re-oxidation.

4. Conclusions

The hydrogen production from water-splitting using solar-driven thermochemical redox cycles based on metal oxide reactions is an attractive route for sustainable and carbon-neutral solar fuel generation. Such cycles involve endothermic reactions that make use of concentrated solar radiation as external heat source for supplying high-temperature process energy. Thermochemical water-splitting processes efficiently convert concentrated solar energy into storable and transportable clean fuels. Concentrating high-flux solar technologies including solar towers and parabolic dishes are already applied at large-scale for commercial electricity and power generation. They may be further coupled to chemical reactors for solar fuel production with potential solar-to-fuel energy conversion efficiencies exceeding 20–25%. Therefore, thermochemical redox cycles should represent an attractive pathway for solar fuels production at competitive costs while further outperforming benchmark water electrolysis process using solar electricity generated by photovoltaics (PV) or concentrating solar power (CSP).

In contrast to the direct thermolysis of H_2O above 2500 °C, thermochemical water-splitting cycles proceed at lower maximum operating temperatures and produce both H_2 and O_2 in separate steps, thereby avoiding their recombination and bypassing the need for high-temperature and costly downstream gas separation. Promising systems under investigation include two-step cycles based on metal oxide redox pairs. The feasibility of solar chemical reactor technologies for the thermal dissociation of volatile oxides (ZnO, SnO_2) was demonstrated and the necessity to operate at reduced pressure under low oxygen partial pressure or to implement gas quenching was especially highlighted to avoid recombination between reduced species and oxygen, and to reach significant oxide conversions. Non-volatile metal oxides cycles (Fe_3O_4/FeO, CeO_2/Ce_2O_3, Ce- and Fe-based mixed oxides, and perovskites) can be operated with continuous removal/separation of the evolved O_2 from the condensed reduced phase during the solar reduction step, so that high reduction extents/rates may be expected without requiring any quenching step. The reduction step proceeds with the material remaining in the condensed state and the evolved O_2 can be released and swept by a flow of inert gas, thus avoiding recombination issues. Non-stoichiometric oxides ($CeO_{2-\delta}$, $ABO_{3-\delta}$) have been considered for decreasing the temperature of the reduction step below 1400 °C, in turn alleviating material sintering and implying enhanced performance stability and cyclability. In contrast to the zinc and tin-based systems, ceria and perovskites remain in the solid state with their crystalline structure maintained stable throughout. Identification of materials formulations with improved redox activity, high oxygen transport and exchange properties, and long-term stability over extended cyclic operation under concentrated solar irradiation is required, as well as their relevant shaping as 3D porous structures capable to absorb concentrated solar radiation while offering large available geometrical surface area for the solid/gas reactions. Such materials can be integrated in monolithic solar reactors

with enhanced efficiency and scalability for future application, in which O_2 and H_2 are produced by temperature-swing cyclic operation through sequential reduction and oxidation steps. Development of solar reactors incorporating heat recuperation between the reduction and oxidation steps is also challenging to help improving the overall energy conversion efficiency. The current scientific and technical challenges for developing clean and efficient H_2 production processes based on innovative two-step cycles are thus related to various research areas involving materials science and chemistry, solar reactors and process engineering.

Funding: This research was partly funded by French National Research Agency (ANR, grant number ANR-09-JCJC-0004-01 and ANR-16-CE06-0010).

Conflicts of Interest: The authors declare no conflict of interest. The funders had no role in the design of the study; in the collection, analyses, or interpretation of data; in the writing of the manuscript, or in the decision to publish the results.

References

1. Yadav, D.; Banerjee, R. A review of solar thermochemical processes. *Renew. Sustain. Energy Rev.* **2016**, *54*, 497–532. [CrossRef]
2. Yilmaz, F.; Tolga Balta, M.; Selbaş, R. A review of solar based hydrogen production methods. *Renew. Sustain. Energy Rev.* **2016**, *56*, 171–178. [CrossRef]
3. Villafán-Vidales, H.I.; Arancibia-Bulnes, C.A.; Riveros-Rosas, D.; Romero-Paredes, H.; Estrada, C.A. An overview of the solar thermochemical processes for hydrogen and syngas production: Reactors, and facilities. *Renew. Sustain. Energy Rev.* **2017**, *75*, 894–908. [CrossRef]
4. Agrafiotis, C.; Roeb, M.; Sattler, C. A review on solar thermal syngas production via redox pair-based water/carbon dioxide splitting thermochemical cycles. *Renew. Sustain. Energy Rev.* **2015**, *42*, 254–285. [CrossRef]
5. Beghi, G.E. A decade of research on thermochemical hydrogen at the Joint Research Centre, Ispra. *Int. J. Hydrogen Energy* **1986**, *11*, 761–771. [CrossRef]
6. Funk, J.E. Thermochemical hydrogen production: Past and present. *Int. J. Hydrogen Energy* **2001**, *16*, 185–190. [CrossRef]
7. Yalcin, S. A review of nuclear hydrogen production. *Int. J. Hydrogen Energy* **1989**, *14*, 551–561. [CrossRef]
8. Bamberger, C.E.; Richardson, D.M. Hydrogen production from water by thermochemical cycles. *Cryogenics* **1976**, *16*, 197–208. [CrossRef]
9. Bamberger, C.E. Hydrogen production from water by thermochemical cycles; A 1977 update. *Cryogenics* **1978**, *18*, 170–183. [CrossRef]
10. Brown, L.C.; Besenbruch, G.E.; Lentsch, R.D.; Schultz, K.R.; Funk, J.F.; Pickard, P.S.; Marshall, A.C.; Showalter, S.K. *High Efficiency Generation of Hydrogen Fuels Using Nuclear Power*; GA-A24285; General Atomics: San Diego, CA, USA, December 2003.
11. Kameyama, H.; Yoshida, K. Reactor design for the UT-3 thermochemical hydrogen production process. *Int. J. Hydrogen Energy* **1981**, *6*, 567–575. [CrossRef]
12. Kameyama, H.; Tomino, Y.; Sato, T.; Amir, R.; Orihara, A.; Aihara, M.; Yoshida, K. Process simulation of 'MASCOT' plant using the UT-3 thermochemical cycle for hydrogen production. *Int. J. Hydrogen Energy* **1989**, *14*, 323–330. [CrossRef]
13. O'Keefe, D.; Allen, C.; Besenbruch, G.; Brown, L.; Norman, J.; Sharp, R.; McCorkle, K. Preliminary results from bench-scale testing of a sulfur-iodine thermochemical water-splitting cycle. *Int. J. Hydrogen Energy* **1982**, *7*, 381–392. [CrossRef]
14. Oztürk, I.T.; Hammache, A.; Bilgen, E. An improved process for H_2SO_4 decomposition step of the sulfur-iodine cycle. *Energy Convers. Mgmt.* **1995**, *36*, 11–21. [CrossRef]
15. Kubo, S.; Nakajima, H.; Kasahara, S.; Higashi, S.; Masaki, T.; Abe, H.; Onuki, K. A demonstration study on a close-cycle hydrogen production by the thermochemical water-splitting iodine-sulfur process. *Nucl. Eng. Design* **2004**, *233*, 347–354. [CrossRef]
16. Kubo, S.; Kasahara, S.; Okuda, H.; Terada, A.; Tanaka, N.; Inaba, Y.; Ohashi, H.; Inagaki, Y.; Onuki, K.; Hino, R. A pilot test plan of the water-splitting iodine-sulfur process. *Nucl. Eng. Design* **2004**, *233*, 355–362. [CrossRef]

17. Noglik, A.; Roeb, M.; Rzepczyk, T.; Hinkley, J.; Sattler, C.; Pitz-Paal, R. Solar Thermochemical Generation of Hydrogen: Development of a Receiver Reactor for the Decomposition of Sulfuric Acid. *J. Sol. Energy Eng.* **2009**, *131*, 011003. [CrossRef]
18. Kolb, G.J.; Diver, R.B.; Siegel, N. Central-Station Solar Hydrogen Power Plant. *J. Sol. Energy Eng.* **2007**, *129*, 179–183. [CrossRef]
19. Bilgen, C.; Broggi, A.; Bilgen, E. The solar Cristina process for hydrogen production. *Sol. Energy* **1986**, *36*, 267–280. [CrossRef]
20. Sakurai, M.; Bilgen, E.; Tsutsumi, A.; Yoshida, K. Adiabatic UT-3 thermochemical process for hydrogen production. *Int. J. Hydrogen Energy* **1996**, *21*, 865–870. [CrossRef]
21. Sakurai, M.; Miyake, N.; Tsutsumi, A.; Yoshida, K. Analysis of a reaction mechanism in the UT-3 thermochemical hydrogen production cycle. *Int. J. Hydrogen Energy* **1996**, *21*, 871–875. [CrossRef]
22. Sakurai, M.; Bilgen, E.; Tsutsumi, A.; Yoshida, K. Solar UT-3 thermochemical cycle for hydrogen production. *Sol. Energy* **1996**, *57*, 51–58. [CrossRef]
23. Graf, D.; Monnerie, N.; Roeb, M.; Schmitz, M.; Sattler, C. Economic comparison of solar hydrogen generation by means of thermochemical cycles and electrolysis. *Int. J. Hydrogen Energy* **2008**, *33*, 4511–4519. [CrossRef]
24. Pregger, T.; Graf, D.; Krewitt, W.; Sattler, C.; Roeb, M.; Möller, S. Prospects of solar thermal hydrogen production processes. *Int. J. Hydrogen Energy* **2009**, *34*, 4256–4267. [CrossRef]
25. Bilgen, E.; Bilgen, C. Solar hydrogen production using two-step thermochemical cycles. *Int. J. Hydrogen Energy* **1982**, *7*, 637–644. [CrossRef]
26. Steinfeld, A.; Kuhn, P.; Reller, A.; Palumbo, R.; Murray, J.; Tamaura, Y. Solar-processed metals as clean energy carriers and water-splitters. *Int. J. Hydrogen Energy* **1998**, *23*, 767–774. [CrossRef]
27. Abanades, S. Hydrogen production technologies from solar thermal energy. *Green* **2011**, *1*, 209–220. [CrossRef]
28. Abanades, S.; Charvin, P.; Flamant, G.; Neveu, P. Screening of water-splitting thermochemical cycles potentially attractive for hydrogen production by concentrated solar energy. *Energy* **2006**, *31*, 2805–2822. [CrossRef]
29. Charvin, P.; Abanades, S.; Lemort, F.; Flamant, G. Analysis of solar processes for hydrogen production from water-splitting thermochemical cycles. *Energy Convers. Manag.* **2008**, *49*, 1547–1556. [CrossRef]
30. Romero, M.; Buck, R.; Pacheco, J.E. An update on solar central receiver systems, projects, and technologies. *J. Sol. Energy Eng.* **2002**, *124*, 98–108. [CrossRef]
31. Dokiya, M.; Kotera, Y. Hybrid cycle with electrolysis using Cu-Cl system. *Int. J. Hydrogen Energy* **1976**, *1*, 117–127. [CrossRef]
32. Wentorf, R.H.; Hanneman, R.E. Thermochemical hydrogen generation. *Science* **1974**, *185*, 311–319. [CrossRef] [PubMed]
33. Ducarroir, M.; Tmar, M.; Bernard, C. Possibilités de stockage de l'énergie solaire à partir de sulfates. *Revue Phys. Appl.* **1980**, *15*, 513–528. [CrossRef]
34. Kameyama, H.; Yoshida, K.; Kunii, D. A method for screening possible thermochemical decomposition processes for water using ΔG^0 -T diagrams. *Chem. Eng. J.* **1976**, *11*, 223–229. [CrossRef]
35. Lundberg, M. Model calculations on some feasible two-step water splitting processes. *Int. J. Hydrogen Energy* **1993**, *18*, 369–376. [CrossRef]
36. Knoche, K.F.; Cremer, H.; Steinborn, G.; Schneider, W. Feasibility studies of chemical reactions for thermochemical water splitting cycles of the iron-chlorine, iron-sulfur and manganese-sulfur families. *Int. J. Hydrogen Energy* **1977**, *2*, 269–289. [CrossRef]
37. Knoche, K.F.; Schuster, P. Thermochemical production of hydrogen by a vanadium/chlorine cycle. Part 1: An energy and exergy analysis of the process. *Int. J. Hydrogen Energy* **1984**, *9*, 457–472. [CrossRef]
38. Knoche, K.F.; Cremer, H.; Steinborn, G. A thermochemical process for hydrogen production. *Int. J. Hydrogen Energy* **1976**, *1*, 23–32. [CrossRef]
39. Ambriz, J.J.; Sibieude, F.; Ducarroir, M. Preparation of cadmium by thermal dissociation of CdO using solar energy. *Int. J. Hydrogen Energy* **1982**, *7*, 143–153. [CrossRef]
40. Steinfeld, A. Solar hydrogen production via a two-step water-splitting thermochemical cycle based on Zn/ZnO redox reactions. *Int. J. Hydrogen Energy* **2002**, *27*, 611–619. [CrossRef]
41. Palumbo, R.; Ledé, J.; Boutin, O.; Elorza Ricart, E.; Steinfeld, A.; Muller, S.; Weidenkaff, A.; Fletcher, E.A.; Bielicki, J. The production of Zn from ZnO in a high-temperature solar decomposition quench process. I—The Scientific framework for the process. *Chem. Eng. Sci.* **1998**, *53*, 2503–2517. [CrossRef]

42. Weidenkaff, A.; Steinfeld, A.; Wokaun, A.; Auer, P.O.; Eichler, B.; Reller, A. Direct solar thermal dissociation of zinc oxide: Condensation and crystallization of zinc in the presence of oxygen. *Sol. Energy* **1999**, *65*, 59–69. [CrossRef]
43. Weidenkaff, A.; Reller, A.W.; Wokaun, A.; Steinfeld, A. Thermogravimetric analysis of the ZnO/Zn water splitting cycle. *Thermochimica Acta* **2000**, *359*, 69–75. [CrossRef]
44. Möller, S.; Palumbo, R. Solar thermal decomposition kinetics of ZnO in the temperature range 1950–2400 K. *Chem. Eng. Sci.* **2001**, *56*, 4505–4515. [CrossRef]
45. Möller, S.; Palumbo, R. The development of a solar chemical reactor for the direct thermal dissociation of zinc oxide. *ASME J. Sol. Energy Eng.* **2001**, *123*, 83–90. [CrossRef]
46. Abanades, S.; Charvin, P.; Flamant, G. Design and simulation of a solar chemical reactor for the thermal reduction of metal oxides: Case study of zinc oxide dissociation. *Chem. Eng. Sci.* **2007**, *62*, 6323–6333. [CrossRef]
47. Chambon, M.; Abanades, S.; Flamant, G. Design of a lab-scale rotary cavity-type solar reactor for continuous thermal reduction of volatile oxides under reduced pressure. *ASME J. Sol. Energy Eng.* **2010**, *132*, 021006. [CrossRef]
48. Chambon, M.; Abanades, S.; Flamant, G. Thermal dissociation of compressed ZnO and SnO_2 powders in a moving front solar thermochemical reactor. *AIChE J.* **2011**, *57*, 2264–2273. [CrossRef]
49. Chambon, M.; Abanades, S.; Flamant, G. Solar Thermal Reduction of ZnO and SnO_2: Characterization of the Recombination Reaction with O_2. *Chem. Eng. Sci.* **2010**, *65*, 3671–3680. [CrossRef]
50. Levêque, G.; Abanades, S. Kinetic analysis of high-temperature solid–gas reactions by an inverse method applied to ZnO and SnO_2 solar thermal dissociation. *Chem. Eng. J.* **2013**, *217*, 139–149. [CrossRef]
51. Charvin, P.; Abanades, S.; Neveu, P.; Lemort, F.; Flamant, G. Dynamic modeling of a volumetric solar reactor for volatile metal oxide reduction. *Chem. Eng. Res. Design* **2008**, *86*, 1216–1222. [CrossRef]
52. Schunk, L.O.; Steinfeld, A. Kinetics of the thermal dissociation of ZnO exposed to concentrated solar irradiation using a solar-driven thermogravimeter in the 1800–2100 K range. *AIChE J.* **2009**, *55*, 1497–1504. [CrossRef]
53. Perkins, C.; Lichty, P.; Weimer, A.W. Determination of aerosol kinetics of thermal ZnO dissociation by thermogravimetry. *Chem. Eng. Sci.* **2007**, *62*, 5952–5962. [CrossRef]
54. Perkins, C.; Lichty, P.R.; Weimer, A.W. Thermal ZnO dissociation in a rapid aerosol reactor as part of a solar hydrogen production cycle. *Int. J. Hydrogen Energy* **2008**, *33*, 499–510. [CrossRef]
55. Melchior, T.; Perkins, C.; Weimer, A.W.; Steinfeld, A. A cavity-receiver containing a tubular absorber for high-temperature thermochemical processing using concentrated solar energy. *Int. J. Therm. Sci.* **2008**, *47*, 1496–1503. [CrossRef]
56. Haussener, S.; Hirsch, D.; Perkins, C.; Weimer, A.; Lewandowski, A.; Steinfeld, A. Modeling of a Multitube High-Temperature Solar Thermochemical Reactor for Hydrogen Production. *J. Sol. Energy Eng.* **2009**, *131*, 024503. [CrossRef]
57. Haueter, P.; Moeller, S.; Palumbo, R.; Steinfeld, A. The production of zinc by thermal dissociation of zinc oxide-Solar chemical reactor design. *Sol. Energy* **1999**, *67*, 161–167. [CrossRef]
58. Muller, R.; Haeberling, P.; Palumbo, R. Further advances toward the development of a direct heating solar thermal chemical reactor for the thermal dissociation of ZnO(s). *Sol. Energy* **2006**, *80*, 500–511. [CrossRef]
59. Schunk, L.; Haeberling, P.; Wepf, S.; Wuillemin, D.; Meier, A.; Steinfeld, A. A Solar Receiver-Reactor for the Thermal Dissociation of Zinc Oxide. *ASME J. Sol. Energy Eng.* **2008**, *130*, 021009. [CrossRef]
60. Koepf, E.; Villasmil, W.; Meier, A. Pilot-scale solar reactor operation and characterization for fuel production via the Zn/ZnO thermochemical cycle. *Appl. Energy* **2016**, *165*, 1004–1023. [CrossRef]
61. Müller, R.; Steinfeld, A. H_2O-splitting thermochemical cycle based on ZnO/Zn-redox: Quenching the effluents from the ZnO dissociation. *Chem. Eng. Sci.* **2008**, *63*, 217–227. [CrossRef]
62. Keunecke, M.; Meier, A.; Palumbo, R. Solar thermal decomposition of zinc oxide: An initial investigation of the recombination reaction in the temperature range 1100–1250 K. *Chem. Eng. Sci.* **2004**, *59*, 2695–2704. [CrossRef]
63. Berman, A.; Epstein, M. The kinetics of hydrogen production in the oxidation of liquid zinc with water vapor. *Int. J. Hydrogen Energy* **2000**, *25*, 957–967. [CrossRef]

64. Wegner, K.; Ly, H.C.; Weiss, R.J.; Pratsinis, S.E.; Steinfeld, A. In situ formation and hydrolysis of Zn nanoparticles for H_2 production by the 2-step ZnO/Zn water-splitting thermochemical cycle. *Int. J. Hydrogen Energy* **2006**, *31*, 55–61. [CrossRef]
65. Weiss, R.J.; Ly, H.C.; Wegner, K.; Pratsinis, S.E.; Steinfeld, A. H_2 production by Zn hydrolysis in a hot-wall aerosol reactor. *AIChE J.* **2005**, *51*, 1966–1970. [CrossRef]
66. Ernst, F.O.; Tricoli, A.; Pratsinis, S.E.; Steinfeld, A. Co-synthesis of H_2 and ZnO by in-situ Zn aerosol formation and hydrolysis. *AIChE J.* **2006**, *52*, 3297–3303. [CrossRef]
67. Melchior, T.; Piatkowski, N.; Steinfeld, A. H_2 production by steam-quenching of Zn vapor in a hot-wall aerosol flow reactor. *Chem. Eng. Sci.* **2009**, *64*, 1095–1101. [CrossRef]
68. Abu Hamed, T.; Davidson, J.H.; Stolzenburg, M. Hydrolysis of Evaporated Zn in a Hot Wall Flow Reactor. *J. Sol. Energy Eng.* **2008**, *130*, 041010. [CrossRef]
69. Lindemer, M.D.; Advani, S.G.; Prasad, A.K. Experimental investigation of heterogeneous hydrolysis with Zn vapor under a temperature gradient. *Int. J. Hydrogen Energy* **2017**, *42*, 7847–7856. [CrossRef]
70. Weibel, D.; Jovanovic, Z.R.; Gálvez, E.; Steinfeld, A. Mechanism of Zn Particle Oxidation by H_2O and CO_2 in the Presence of ZnO. *Chem. Mater.* **2014**, *26*, 6486–6495. [CrossRef]
71. Ernst, F.O.; Steinfeld, A.; Pratsinis, S.E. Hydrolysis rate of submicron Zn particles for solar H_2 synthesis. *Int. J. Hydrogen Energy* **2009**, *34*, 1166–1175. [CrossRef]
72. Funke, H.H.; Diaz, H.; Liang, X.; Carney, C.S.; Weimer, A.W.; Li, P. Hydrogen generation by hydrolysis of zinc powder aerosol. *Int. J. Hydrogen Energy* **2008**, *33*, 1127–1134. [CrossRef]
73. Vishnevetsky, I.; Epstein, M. Production of hydrogen from solar zinc in steam atmosphere. *Int. J. Hydrogen Energy* **2007**, *32*, 2791–2802. [CrossRef]
74. Abanades, S. Thermogravimetry analysis of CO_2 and H_2O reduction from solar nanosized Zn powder for thermochemical fuel production. *Ind. Eng. Chem. Res.* **2012**, *51*, 741–750. [CrossRef]
75. Villafán-Vidales, H.I.; Abanades, S.; Montiel-González, M.; Romero-Paredes, H.; Arancibia-Bulnes, C.A.; Estrada, C.A. Transient heat transfer simulation of a 1 kW_{th} moving front solar thermochemical reactor for thermal dissociation of compressed ZnO. *Chem. Eng. Res. Design* **2015**, *93*, 174–184. [CrossRef]
76. Levêque, G.; Abanades, S. Investigation of thermal and carbothermal reduction of volatile oxides (ZnO, SnO_2, GeO_2, and MgO) via solar-driven vacuum thermogravimetry for thermochemical production of solar fuels. *Thermochimica Acta* **2015**, *605*, 86–94. [CrossRef]
77. Abanades, S.; Charvin, P.; Lemont, F.; Flamant, G. Novel two-step SnO_2/SnO water-splitting cycle for solar thermochemical production of hydrogen. *Int. J. Hydrogen Energy* **2008**, *33*, 6021–6030. [CrossRef]
78. Charvin, P.; Abanades, S.; Lemont, F.; Flamant, G. Experimental study of SnO_2/SnO/Sn thermochemical systems for solar production of hydrogen. *AIChE J.* **2008**, *54*, 2759–2767. [CrossRef]
79. Chambon, M.; Abanades, S.; Flamant, G. Kinetic investigation of hydrogen generation from hydrolysis of SnO and Zn solar nanopowders. *Int. J. Hydrogen Energy* **2009**, *34*, 5326–5336. [CrossRef]
80. Abanades, S. CO_2 and H_2O reduction by solar thermochemical looping using SnO_2/SnO redox reactions: Thermogravimetric analysis. *Int. J. Hydrogen Energy* **2012**, *37*, 8223–8231. [CrossRef]
81. Levêque, G.; Abanades, S.; Jumas, J.-C.; Olivier-Fourcade, J. Characterization of two-step tin-based redox system for thermochemical fuel production from solar-driven CO_2 and H_2O splitting cycle. *Ind. Eng. Chem. Res.* **2014**, *53*, 5668–5677. [CrossRef]
82. Levêque, G.; Abanades, S. Thermodynamic and kinetic study of the carbothermal reduction of SnO_2 for solar thermochemical fuel generation. *Energy Fuels* **2014**, *28*, 1396–1405. [CrossRef]
83. Sturzenegger, M.; Nuesch, P. Efficiency analysis for a manganese-oxide-based thermochemical cycle. *Energy* **1999**, *24*, 959–970. [CrossRef]
84. Abanades, S.; Flamant, G. Thermochemical hydrogen production from a two-step solar-driven water-splitting cycle based on cerium oxides. *Sol. Energy* **2006**, *80*, 1611–1623. [CrossRef]
85. Charvin, P.; Abanades, S.; Bêche, E.; Lemont, F.; Flamant, G. Hydrogen production from mixed cerium oxides via three-step water-splitting cycles. *Solid State Ionics* **2009**, *180*, 1003–1010. [CrossRef]
86. Bamberger, C.E.; Nichols, H. Basic chemistry of a new cycle, based on reactions of Ce(III) titanate, for splitting water. *Int. J. Hydrogen Energy* **1979**, *4*, 513–516. [CrossRef]
87. Nakamura, T. Hydrogen production from water utilizing solar heat at high temperatures. *Sol. Energy* **1977**, *19*, 467–475. [CrossRef]

88. Sibieude, F.; Ducarroir, M.; Tofighi, A.; Ambriz, J. High temperature experiments with a solar furnace. The decomposition of Fe_3O_4, Mn_3O_4, CdO. *Int. J. Hydrogen Energy* **1982**, *7*, 79–88. [CrossRef]
89. Tofighi, A.; Sibieude, F.; Ducarroir, M.; Benezech, G. Thermal decomposition of magnetite in air at the focus of a solar furnace (Décomposition thermique à l'air de la magnétite au foyer d'un four solaire). *Rev. Int. Htes Temp. Réfract.* **1978**, *15*, 7–14.
90. Tofighi, A.; Sibieude, F. Dissociation of magnetite in a solar furnace for hydrogen production. Tentative production evaluation of a 1000 kW concentrator from small scale (2 kW) experimental results. *Int. J. Hydrogen Energy* **1984**, *9*, 293–296. [CrossRef]
91. Steinfeld, A.; Sanders, S.; Palumbo, R. Design aspects of solar thermochemical engineering—A case study: Two-step water-splitting cycle using the Fe_3O_4/FeO redox system. *Sol. Energy* **1999**, *65*, 43–53. [CrossRef]
92. Weidenkaff, A.; Nüesch, P.; Wokaun, A.; Reller, A. Mechanistic studies of the water-splitting reaction for producing solar hydrogen. *Solid State Ionics* **1997**, *101–103*, 915–922. [CrossRef]
93. Charvin, P.; Abanades, S.; Flamant, G.; Lemort, F. Two-step water-splitting thermochemical cycle based on iron oxide redox pair for solar hydrogen production. *Energy* **2007**, *32*, 1124–1133. [CrossRef]
94. Charvin, P.; Abanades, S.; Lemort, F.; Flamant, G. Hydrogen production by three-step solar thermochemical cycles using hydroxides and metal oxide systems. *Energy Fuels* **2007**, *21*, 2919–2928. [CrossRef]
95. Ehrensberger, K.; Frei, A.; Kuhn, P.; Oswald, H.; Hug, P. Comparative experimental investigations of the water splitting reaction with iron oxide $Fe_{1-y}O$ and iron manganese oxides $(Fe_{1-x}Mn_x)_{1-y}O$. *Solid State Ionics* **1995**, *78*, 151–160. [CrossRef]
96. Tamaura, Y.; Steinfeld, A.; Kuhn, P.; Ehrensberger, K. Production of solar hydrogen by a novel, 2-step, water-splitting thermochemical cycle. *Energy* **1995**, *20*, 325–330. [CrossRef]
97. Tamaura, Y.; Ueda, Y.; Matsunami, J.; Hasegawa, N.; Nesuka, M.; Sano, T.; Tsuji, M. Solar hydrogen production by using ferrites. *Sol. Energy* **1999**, *65*, 55–57. [CrossRef]
98. Tamaura, Y.; Kojima, M.; Sano, Y.; Ueda, Y.; Hasegawa, N.; Tsuji, M. Thermodynamic evaluation of water splitting by a cation excessive (Ni, Mn) ferrite. *Int. J. Hydrogen Energy* **1998**, *23*, 1185–1191. [CrossRef]
99. Inoue, M.; Hasegawa, N.; Uehara, R.; Gokon, N.; Kaneko, H.; Tamaura, Y. Solar hydrogen generation with H_2O/ZnO/$MnFe_2O_4$ system. *Sol. Energy* **2004**, *76*, 309–315. [CrossRef]
100. Kaneko, H.; Hosokawa, Y.; Kojima, N.; Gokon, N.; Hasegawa, N.; Kitamura, M.; Tamaura, Y. Studies on metal oxides suitable for enhancement of the O_2-releasing step in water splitting by the $MnFe_2O_4$–Na_2CO_3 system. *Energy* **2001**, *26*, 919–929. [CrossRef]
101. Kaneko, H.; Hosokawa, Y.; Gokon, N.; Kojima, N.; Hasegawa, N.; Kitamura, M.; Tamaura, Y. Enhancement of O_2-releasing step with Fe_2O_3 in the water splitting by $MnFe_2O_4$–Na_2CO_3 system. *J. Phys. Chem. Solids* **2001**, *62*, 1341–1347. [CrossRef]
102. Kaneko, H.; Ochiai, Y.; Shimizu, K.; Hosokawa, Y.; Gokon, N.; Tamaura, Y. Thermodynamic study based on the phase diagram of the Na_2O–MnO–Fe_2O_3 system for H_2 production in three-step water splitting with Na_2CO_3/$MnFe_2O_4$/Fe_2O_3. *Sol. Energy* **2002**, *72*, 377–383. [CrossRef]
103. Kaneko, H.; Gokon, N.; Hasegawa, N.; Tamaura, Y. Solar thermochemical process for hydrogen production using ferrites. *Energy* **2005**, *30*, 2171–2178. [CrossRef]
104. Tamaura, Y.; Kojima, N.; Hasegawa, N.; Inoue, M.; Uehara, R.; Gokon, N.; Kaneko, H. Stoichiometric studies of H_2 generation reaction for H_2O/Zn/Fe_3O_4 system. *Int. J. Hydrogen Energy* **2001**, *26*, 917–922. [CrossRef]
105. Tamaura, Y.; Kaneko, H. Oxygen-releasing step of $ZnFe_2O_4$/(ZnO + Fe_3O_4)-system in air using concentrated solar energy for solar hydrogen production. *Sol. Energy* **2005**, *78*, 616–622. [CrossRef]
106. Takahashi, Y.; Aoki, H.; Kaneko, H.; Hasegawa, N.; Suzuki, A.; Tamaura, Y. Oxygen-gas-releasing reaction of Zn ferrite by Xe lamp beam irradiation in air at 1800 K. *Solid State Ionics* **2004**, *172*, 89–91. [CrossRef]
107. Aoki, H.; Kaneko, H.; Hasegawa, N.; Ishihara, H.; Suzuki, A.; Tamaura, Y. The $ZnFe_2O_4$/(ZnO+Fe_3O_4) system for H_2 production using concentrated solar energy. *Solid State Ionics* **2004**, *172*, 113–116. [CrossRef]
108. Tamaura, Y.; Uehara, R.; Hasegawa, N.; Kaneko, H.; Aoki, H. Study on solid-state chemistry of the ZnO/Fe_3O_4/H_2O system for H_2 production at 973–1073 K. *Solid State Ionics* **2004**, *172*, 121–124. [CrossRef]
109. Kaneko, H.; Kojima, N.; Hasegawa, N.; Inoue, M.; Uehara, R.; Gokon, N.; Tamaura, Y.; Sano, T. Reaction mechanism of H_2 generation for H_2O/Zn/Fe_3O_4 system. *Int. J. Hydrogen Energy* **2002**, *27*, 1023–1028. [CrossRef]
110. Kaneko, H.; Kodama, T.; Gokon, N.; Tamaura, Y.; Lovegrove, K.; Luzzi, A. Decomposition of Zn-ferrite for O_2 generation by concentrated solar radiation. *Sol. Energy* **2004**, *76*, 317–322. [CrossRef]

111. Ishihara, H.; Hasegawa, N.; Aoki, H.; Kaneko, H.; Suzuki, A.; Tamaura, Y. Two-step water splitting for H_2 production with Zn^{II}-$Mn^{II,III}$-Fe^{III} spinel structure using concentrated solar heat. *Solid States Ionics* **2004**, *172*, 117–119. [CrossRef]
112. Ishihara, H.; Kaneko, H.; Hasegawa, N.; Tamaura, Y. Two-step water-splitting at 1273–1623 K using yttria-stabilized zirconia-iron oxide solid solution via co-precipitation and solid-state reaction. *Energy* **2008**, *33*, 1788–1793. [CrossRef]
113. Kaneko, H.; Yokoyama, T.; Fuse, A.; Ishihara, H.; Hasegawa, N.; Tamaura, Y. Synthesis of new ferrite, Al–Cu ferrite, and its oxygen deficiency for solar H_2 generation from H_2O. *Int. J. Hydrogen Energy* **2006**, *31*, 2256–2265. [CrossRef]
114. Kodama, T.; Kondoh, Y.; Yamamoto, R.; Andou, H.; Satou, N. Thermochemical hydrogen production by a redox system of ZrO_2-supported Co(II)-ferrite. *Sol. Energy* **2005**, *78*, 623–631. [CrossRef]
115. Kodama, T.; Gokon, N.; Yamamoto, R. Thermochemical two-step water splitting by ZrO_2-supported $Ni_xFe_{3-x}O_4$ for solar hydrogen production. *Sol. Energy* **2008**, *82*, 73–79. [CrossRef]
116. Gokon, N.; Murayama, H.; Umeda, J.; Hatamachi, T.; Kodama, T. Monoclinic zirconia-supported Fe_3O_4 for the two-step water-splitting thermochemical cycle at high thermal reduction temperatures of 1400–1600 °C. *Int. J. Hydrogen Energy* **2009**, *34*, 1208–1217. [CrossRef]
117. Gokon, N.; Murayama, H.; Nagasaki, A.; Kodama, T. Thermochemical two-step water splitting cycles by monoclinic ZrO_2-supported $NiFe_2O_4$ and Fe_3O_4 powders and ceramic foam devices. *Sol. Energy* **2009**, *83*, 527–537. [CrossRef]
118. Gokon, N.; Hasegawa, T.; Takahashi, S.; Kodama, T. Thermochemical two-step water-splitting for hydrogen production using Fe-YSZ particles and a ceramic foam device. *Energy* **2008**, *33*, 1407–1416. [CrossRef]
119. Gokon, N.; Takahashi, S.; Yamamoto, H.; Kodama, T. Thermochemical two-step water-splitting reactor with internally circulating fluidized bed for thermal reduction of ferrite particles. *Int. J. Hydrogen Energy* **2008**, *33*, 2189–2199. [CrossRef]
120. Kaneko, H.; Miura, T.; Fuse, A.; Ishihara, H.; Taku, S.; Fukuzumi, H.; Naganuma, Y.; Tamaura, Y. Rotary-Type Solar Reactor for Solar Hydrogen Production with Two-step Water Splitting Process. *Energy Fuels* **2007**, *21*, 2287–2293. [CrossRef]
121. Han, S.B.; Kang, T.B.; Joo, O.S.; Jung, K.D. Water splitting for hydrogen production with ferrites. *Sol. Energy* **2007**, *81*, 623–628. [CrossRef]
122. Roeb, M.; Sattler, C.; Klüser, R.; Monnerie, N.; de Oliveira, L.; Konstandopoulos, A.G.; Agrafiotis, C.; Zaspalis, V.T.; Nalbandian, L.; Steele, A.; et al. Solar Hydrogen Production by a Two-Step Cycle Based on Mixed Iron Oxides. *J. Sol. Energy Eng.* **2006**, *128*, 125–133. [CrossRef]
123. Roeb, M.; Neises, M.; Säck, J.-P.; Rietbrock, P.; Monnerie, N.; Dersch, J.; Schmitz, M.; Sattler, C. Operational strategy of a two-step thermochemical process for solar hydrogen production. *Int. J. Hydrogen Energy* **2009**, *34*, 4537–4545. [CrossRef]
124. Agrafiotis, C.; Roeb, M.; Konstandopoulos, A.G.; Nalbandian, L.; Zaspalis, V.T.; Sattler, C.; Stobbe, P.; Steele, A.M. Solar water splitting for hydrogen production with monolithic reactors. *Sol. Energy* **2005**, *79*, 409–421. [CrossRef]
125. Agrafiotis, C.C.; Pagkoura, C.; Lorentzou, S.; Kostoglou, M.; Konstandopoulos, A.G. Hydrogen production in solar reactors. *Catal. Today* **2007**, *127*, 265–277. [CrossRef]
126. Diver, R.B.; Miller, J.E.; Allendorf, M.D.; Siegel, N.P.; Hogan, R.E. Solar Thermochemical Water-Splitting Ferrite-Cycle Heat Engines. *J. Sol. Energy Eng.* **2008**, *130*, 041001. [CrossRef]
127. Allendorf, M.D.; Diver, R.B.; Siegel, N.P.; Miller, J.E. Two-Step Water Splitting Using Mixed-Metal Ferrites: Thermodynamic Analysis and Characterization of Synthesized Materials. *Energy Fuels* **2008**, *22*, 4115–4124. [CrossRef]
128. Fletcher, E.A. Solar thermal and solar quasi-electrolytic processing and separations: Zinc from zinc oxide as an example. *Ind. Eng. Chem. Res.* **1999**, *38*, 2275–2282. [CrossRef]
129. Palumbo, R.D.; Fletcher, E.A. High-temperature solar electrothermal processing. Zinc from zinc-oxide at 1200–1675 K using a non-consumable anode. *Energy* **1988**, *14*, 319–332. [CrossRef]
130. Souriau, D. Procédé et Dispositif pour L'utilisation D'énergie Thermique à Haute Température, en Particulier d'Origine Nucléaire. Device and Method for the Use of High-Temperature Heat Energy, in Particular of Nuclear Origin. Gaz de France Patent FR2135421, 22 December 1972. (In French)

131. Vishnevetsky, I.; Epstein, M. Tin as a Possible Candidate for Solar Thermochemical Redox Process for Hydrogen Production. *J. Sol. Energy Eng.* **2009**, *131*, 021007. [CrossRef]
132. Fletcher, E.A. Solar thermal processing: A review. *J. Sol. Energy Eng.* **2001**, *123*, 63–74. [CrossRef]
133. Kodama, T. High-temperature solar chemistry for converting solar heat to chemical fuels. *Prog. Energy Combust. Sci.* **2003**, *29*, 567–597. [CrossRef]
134. Segal, A.; Epstein, M. The optics of the solar tower reflector. *Sol. Energy* **2000**, *69*, 229–241. [CrossRef]
135. Kaneko, H.; Miura, T.; Ishihara, H.; Taku, S.; Yokoyama, T.; Nakajima, H.; Tamaura, Y. Reactive ceramics of CeO_2-MO_x (M = Mn, Fe, Ni, Cu) for H_2 generation by two-step water splitting using concentrated solar thermal energy. *Energy* **2007**, *32*, 656–663. [CrossRef]
136. Abanades, S.; Legal, A.; Cordier, A.; Peraudeau, G.; Flamant, G.; Julbe, A. Investigation of reactive cerium-based oxides for H_2 production by thermochemical 2-step water-splitting. *J. Mater. Sci.* **2010**, *45*, 4163–4173. [CrossRef]
137. Miller, J.E.; Allendorf, M.D.; Diver, R.B.; Evans, L.R.; Siegel, N.P.; Stuecker, J.N. Metal oxide composites and structures for ultra-high temperature solar thermochemical cycles. *J. Mater. Sci.* **2008**, *43*, 4714–4728. [CrossRef]
138. Chueh, W.; Haile, S.M. A thermochemical study of ceria: Exploiting an old material for new modes of energy conversion and CO_2 mitigation. *Phil. Trans. R. Soc. A* **2010**, *368*, 3269–3294. [CrossRef]
139. Chueh, W.C.; Haile, S.M. Ceria as a Thermochemical Reaction Medium for Selectively Generating Syngas or Methane from H_2O and CO_2. *ChemSusChem* **2009**, *12*, 735–739. [CrossRef]
140. Kaneko, H.; Tamaura, Y. Reactivity and XAFS study on (1−x)CeO_2–xNiO (x = 0.025–0.3) system in the two-step water-splitting reaction for solar H_2 production. *J. Phys. Chem. Solids* **2009**, *70*, 1008–1014. [CrossRef]
141. Kaneko, H.; Ishihara, H.; Taku, S.; Naganuma, Y.; Hasegawa, N.; Tamaura, Y. Cerium ion redox system in CeO_2–xFe_2O_3 solid solution at high temperatures (1,273–1,673 K) in the two-step water-splitting reaction for solar H_2 generation. *J. Mater. Sci.* **2008**, *43*, 3153–3161. [CrossRef]
142. Meng, Q.-L.; Lee, C.-I.; Ishihara, T.; Kaneko, H.; Tamaura, Y. Reactivity of CeO_2 based ceramics for solar hydrogen production via a two-step water-splitting cycle with concentrated energy. *Int. J. Hydrogen Energy* **2011**, *36*, 13435–13441. [CrossRef]
143. Kaneko, H.; Taku, S.; Tamaura, Y. Reduction reactivity of CeO_2-ZrO_2 oxide under high O_2 partial pressure in two-step water-splitting process. *Sol. Energy* **2011**, *85*, 2321–2330. [CrossRef]
144. Lee, C.; Meng, Q.; Kaneko, H.; Tamaura, Y. Solar hydrogen productivity of ceria-scandia solid solution using two-step water-splitting cycle. *J. Sol. Energy Eng.* **2013**, *135*, 11002–11009. [CrossRef]
145. Le Gal, A.; Abanades, S. Catalytic investigation of ceria-zirconia solid solutions for solar hydrogen production. *Int. J. Hydrogen Energy* **2011**, *36*, 4739–4748. [CrossRef]
146. Le Gal, A.; Abanades, S.; Flamant, G. CO_2 and H_2O splitting for thermochemical production of solar fuels using non-stoichiometric ceria and ceria/zirconia solid solutions. *Energy Fuels* **2011**, *25*, 4836–4845. [CrossRef]
147. Le Gal, A.; Abanades, S. Dopant incorporation in ceria for enhanced water-splitting activity during solar thermochemical hydrogen generation. *J. Phys. Chem. C* **2012**, *116*, 13516–13523. [CrossRef]
148. Abanades, S.; Le Gal, A. CO_2 splitting by thermo-chemical looping based on $Zr_xCe_{1-x}O_2$ oxygen carriers for synthetic fuel generation. *Fuel* **2012**, *102*, 180–186. [CrossRef]
149. Le Gal, A.; Abanades, S.; Bion, N.; Le Mercier, T.; Harlé, V. Reactivity of Doped Ceria-Based Mixed Oxides for Solar Thermochemical Hydrogen Generation via Two-Step Water-Splitting Cycles. *Energy Fuels* **2013**, *27*, 6068–6078. [CrossRef]
150. Call, F.; Roeb, M.; Schmücker, M.; Sattler, C.; Pitz-Paal, R. Ceria Doped with Zirconium and Lanthanide Oxides to Enhance Solar Thermochemical Production of Fuels. *J. Phys. Chem. C* **2015**, *119*, 6929–6938. [CrossRef]
151. Bulfin, B.; Call, F.; Vieten, J.; Roeb, M.; Sattler, C.; Shvets, I.V. Oxidation and Reduction Reaction Kinetics of Mixed Cerium Zirconium Oxides. *J. Phys. Chem. C* **2016**, *120*, 2027–2035. [CrossRef]
152. Muhich, C.; Hoes, M.; Steinfeld, A. Mimicking tetravalent dopant behavior using paired charge compensating dopants to improve the redox performance of ceria for thermochemically splitting H_2O and CO_2. *Acta Materialia* **2018**, *144*, 728–737. [CrossRef]
153. Davenport, T.C.; Kemei, M.; Ignatowich, M.J.; Haile, S.M. Interplay of material thermodynamics and surface reaction rate on the kinetics of thermochemical hydrogen production. *Int. J. Hydrogen Energy* **2017**, *42*, 16932–16945. [CrossRef]

154. Petkovich, N.D.; Rudisill, G.; Ventrom, L.J.; Bomant, D.B.; Davidson, J.H.; Stein, A. Control of heterogeneity in nanostructured $Ce_{1-x}Zr_xO_2$ binary oxides for enhanced thermal stability and water splitting activity. *J. Phys. Chem. C* **2011**, *115*, 21022–21033. [CrossRef]
155. Oliveira, F.A.C.; Barreiros, M.A.; Abanades, S.; Caetano, A.P.F.; Novais, R.M.; Pullar, R.C. Solar thermochemical CO_2 splitting using cork-templated ceria ecoceramics. *J. CO2 Util.* **2018**, *26*, 552–563. [CrossRef]
156. Furler, P.; Scheffe, J.R.; Steinfeld, A. Syngas production by simultaneous splitting of H_2O and CO_2 via ceria redox reactions in a high-temperature solar reactor. *Energy Environ. Sci.* **2012**, *5*, 6098–6103. [CrossRef]
157. Gladen, A.C.; Davidson, J.H. The morphological stability and fuel production of commercial fibrous ceria particles for solar thermochemical redox cycling. *Sol. Energy* **2016**, *139*, 524–532. [CrossRef]
158. Furler, P.; Scheffe, J.; Gorbar, M.; Moes, L.; Vogt, U.; Steinfeld, A. Solar thermochemical CO_2 splitting utilizing a reticulated porous ceria redox system. *Energy Fuels* **2012**, *26*, 7051–7059. [CrossRef]
159. Marxer, D.; Furler, P.; Takacs, M.; Steinfeld, A. Solar thermochemical splitting of CO_2 into separate streams of CO and O_2 with high selectivity, stability, conversion, and efficiency. *Energy Environ. Sci.* **2017**, *10*, 1142–1149. [CrossRef]
160. Cho, H.S.; Gokon, N.; Kodama, T.; Kang, Y.H.; Lee, H.J. Improved operation of solar reactor for two-step water-splitting H_2 production by ceria-coated ceramic foam device. *Int. J. Hydrogen Energy.* **2015**, *40*, 114–124. [CrossRef]
161. Scheffe, J.R.; Steinfeld, A. Oxygen exchange materials for solar thermochemical splitting of H_2O and CO_2: A review. *Mater. Today* **2014**, *17*, 341–348. [CrossRef]
162. Carrillo, R.J.; Scheffe, J.R. Advances and trends in redox materials for solar thermochemical fuel production. *Sol. Energy* **2017**, *156*, 3–20. [CrossRef]
163. Roeb, M.; Neises, M.; Monnerie, N.; Call, F.; Simon, H.; Sattler, C.; Schmücker, M.; Pitz-Paal, R. Materials-Related Aspects of Thermochemical Water and Carbon Dioxide Splitting: A Review. *Materials* **2012**, *5*, 2015–2054. [CrossRef]
164. Scheffe, J.R.; Weibel, D.; Steinfeld, A. Lanthanum-strontium-manganese perovskites as redox materials for solar thermochemical splitting of H_2O and CO_2. *Energy Fuels* **2013**, *27*, 4250–4257. [CrossRef]
165. McDaniel, A.H.; Miller, E.C.; Arifin, D.; Ambrosini, A.; Coker, E.N.; O'Hayre, R.; Chueh, W.C.; Tong, J. Sr- and Mn-doped $LaAlO_3$-delta for solar thermochemical H_2 and CO production. *Energy Environ. Sci.* **2013**, *6*, 2424–2428. [CrossRef]
166. Demont, A.; Abanades, S.; Beche, E. Investigation of perovskite structures as oxygen-exchange redox materials for hydrogen production from thermochemical two-step water-splitting cycles. *J. Phys. Chem. C* **2014**, *118*, 12682–12692. [CrossRef]
167. Yang, C.-K.; Yamazaki, Y.; Aydin, A.; Haile, S.M. Thermodynamic and kinetic assessments of strontium-doped lanthanum manganite perovskites for two-step thermochemical water splitting. *J. Mater. Chem. A* **2014**, *2*, 13612–13623. [CrossRef]
168. Demont, A.; Abanades, S. High redox activity of Sr-substituted lanthanum manganite perovskites for two-step thermochemical dissociation of CO_2. *RSC Adv.* **2014**, *4*, 54885–54891. [CrossRef]
169. Demont, A.; Abanades, S. Solar thermochemical conversion of CO_2 into fuel via two-step redox cycling of non-stoichiometric Mn-containing perovskite oxides. *J. Mater. Chem. A* **2015**, *3*, 3536–3546. [CrossRef]
170. Nair, M.M.; Abanades, S. Insights into the Redox Performance of Non-stoichiometric Lanthanum Manganite Perovskites for Solar Thermochemical CO_2 Splitting. *ChemistrySelect* **2016**, *1*, 4449–4457. [CrossRef]
171. Nair, M.M.; Abanades, S. Experimental screening of perovskite oxides as efficient redox materials for solar thermochemical CO_2 conversion. *Sustain. Energy Fuels* **2018**, *2*, 843–854. [CrossRef]
172. Orfila, M.; Linares, M.; Molina, R.; Botas, J.A.; Sanz, R.; Marugan, J. Perovskite materials for hydrogen production by thermochemical water splitting. *Int. J. Hydrogen Energy* **2016**, *41*, 19329–19338. [CrossRef]
173. Haeussler, A.; Abanades, S.; Jouannaux, J.; Julbe, A. Non-stoichiometric redox active perovskite materials for solar thermochemical fuel production: A review. *Catalysts* **2018**, *8*, 611. [CrossRef]